

## Electroproduction of $p\pi^+\pi^-$ off protons at $0.2 < Q^2 < 0.6 \text{ GeV}^2$ and $1.3 < W < 1.57 \text{ GeV}$ with the CLAS detector

G. V. Fedotov,<sup>1</sup> V. I. Mokeev,<sup>1,2</sup> V. D. Burkert,<sup>2</sup> L. Elouadrhiri,<sup>2</sup> E. N. Golovatch,<sup>1</sup> B. S. Ishkhanov,<sup>1</sup> E. L. Isupov,<sup>1</sup> N. V. Shvedunov,<sup>1</sup> G. Adams,<sup>25</sup> M. J. Amarian,<sup>24</sup> P. Ambrozewicz,<sup>11</sup> M. Anghinolfi,<sup>16</sup> B. Asavapibhop,<sup>31</sup> G. Asryan,<sup>39</sup> H. Avakian,<sup>2</sup> H. Baghdasaryan,<sup>24</sup> N. Baillie,<sup>8</sup> J. P. Ball,<sup>3</sup> N. A. Baltzell,<sup>33</sup> V. Batourine,<sup>20</sup> M. Battaglieri,<sup>16</sup> I. Bedlinskiy,<sup>18</sup> M. Bektasoglu,<sup>24</sup> M. Bellis,<sup>4,25</sup> N. Benmouna,<sup>13</sup> A. S. Biselli,<sup>10</sup> B. E. Bonner,<sup>26</sup> S. Bouchigny,<sup>2,15</sup> S. Boiarinov,<sup>2</sup> R. Bradford,<sup>4</sup> D. Branford,<sup>9</sup> W. K. Brooks,<sup>36</sup> S. Bültmann,<sup>24</sup> C. Butuceanu,<sup>8</sup> J. R. Calarco,<sup>32</sup> S. L. Careccia,<sup>24</sup> D. S. Carman,<sup>2</sup> B. Carnahan,<sup>5</sup> S. Chen,<sup>12</sup> P. L. Cole,<sup>2,14</sup> P. Coltharp,<sup>2,12</sup> P. Corvisiero,<sup>16</sup> D. Crabb,<sup>37</sup> H. Crannell,<sup>5</sup> V. Crede,<sup>12</sup> J. P. Cummings,<sup>25</sup> N. B. Dashyan,<sup>39</sup> E. De Sanctis,<sup>17</sup> R. De Vita,<sup>16</sup> P. V. Degtyarenko,<sup>2</sup> H. Denizli,<sup>34</sup> L. Dennis,<sup>12</sup> K. V. Dharmawardane,<sup>24</sup> R. Dickson,<sup>4</sup> C. Djalali,<sup>33</sup> G. E. Dodge,<sup>24</sup> J. Donnelly,<sup>30</sup> D. Doughty,<sup>2,6</sup> M. Dugger,<sup>3</sup> S. Dytman,<sup>34</sup> O. P. Dzyubak,<sup>33</sup> H. Egiyan,<sup>32</sup> K. S. Egiyan,<sup>2,39,\*</sup> P. Eugenio,<sup>12</sup> R. Fatemi,<sup>37</sup> R. J. Feuerbach,<sup>4</sup> T. A. Forest,<sup>24</sup> H. Funsten,<sup>8,\*</sup> G. Gavalian,<sup>24</sup> N. G. Gevorgyan,<sup>39</sup> G. P. Gilfoyle,<sup>35</sup> K. L. Giovanetti,<sup>19</sup> F. X. Girod,<sup>2</sup> J. T. Goetz,<sup>28</sup> R. W. Gothe,<sup>33</sup> K. A. Griffioen,<sup>8</sup> M. Guidal,<sup>15</sup> M. Guillo,<sup>33</sup> N. Guler,<sup>24</sup> L. Guo,<sup>2</sup> V. Gyurjyan,<sup>2</sup> C. Hadjidakis,<sup>15</sup> J. Hardie,<sup>2,6</sup> N. Hassall,<sup>30</sup> F. W. Hersman,<sup>32</sup> K. Hicks,<sup>23</sup> I. Hleiqawi,<sup>23</sup> M. Holtrop,<sup>32</sup> J. Hu,<sup>25</sup> M. Huertas,<sup>33</sup> C. E. Hyde,<sup>24</sup> Y. Ilieva,<sup>13</sup> D. G. Ireland,<sup>30</sup> M. M. Ito,<sup>2</sup> D. Jenkins,<sup>38</sup> H. S. Jo,<sup>15</sup> K. Joo,<sup>29,37</sup> H. G. Juengst,<sup>13</sup> J. D. Kellie,<sup>30</sup> M. Khandaker,<sup>22</sup> K. Y. Kim,<sup>34</sup> K. Kim,<sup>20</sup> W. Kim,<sup>20,24</sup> A. Klein,<sup>20,24</sup> F. J. Klein,<sup>24</sup> A. Klimentenko,<sup>24</sup> M. Klusman,<sup>25</sup> Z. Krahn,<sup>4</sup> L. H. Kramer,<sup>2,11</sup> V. Kubarovsky,<sup>25</sup> J. Kuhn,<sup>4</sup> S. E. Kuhn,<sup>24</sup> S. Kuleshov,<sup>18,36</sup> J. Lachniet,<sup>4</sup> J. M. Laget,<sup>2,7</sup> J. Langheinrich,<sup>33</sup> D. Lawrence,<sup>31</sup> T. Lee,<sup>32</sup> K. Livingston,<sup>30</sup> N. Markov,<sup>29</sup> M. McCracken,<sup>4</sup> B. McKinnon,<sup>30</sup> J. W. C. McNabb,<sup>4</sup> B. A. Mecking,<sup>2</sup> M. D. Mestayer,<sup>2</sup> C. A. Meyer,<sup>4</sup> T. Mibe,<sup>23</sup> K. Mikhailov,<sup>18</sup> T. Mineeva,<sup>29</sup> R. Minehart,<sup>37</sup> M. Mirazita,<sup>17</sup> R. Miskimen,<sup>31</sup> K. Moriya,<sup>4</sup> S. A. Morrow,<sup>7,15</sup> J. Mueller,<sup>34</sup> G. S. Mutchler,<sup>26,\*</sup> P. Nadel-Turonski,<sup>13</sup> R. Nasseripour,<sup>11</sup> S. Niccolai,<sup>13,15</sup> G. Niculescu,<sup>19,23</sup> I. Niculescu,<sup>13,19</sup> B. B. Nizchyporuk,<sup>2</sup> R. A. Niyazov,<sup>2,25</sup> G. V. O'Rielly,<sup>31</sup> M. Osipenko,<sup>1,16</sup> A. I. Ostrovidov,<sup>12</sup> K. Park,<sup>33</sup> E. Pasyuk,<sup>3</sup> C. Paterson,<sup>30</sup> J. Pierce,<sup>37</sup> N. Pivnyuk,<sup>18</sup> D. Pocanic,<sup>37</sup> O. Pogorelko,<sup>18</sup> S. Pozdniakov,<sup>18</sup> J. W. Price,<sup>28</sup> Y. Prok,<sup>2</sup> D. Protopopescu,<sup>30</sup> B. A. Raue,<sup>2,11</sup> G. Ricco,<sup>16</sup> M. Ripani,<sup>16</sup> B. G. Ritchie,<sup>3</sup> G. Rosner,<sup>30</sup> P. Rossi,<sup>17</sup> D. Rowntree,<sup>21</sup> P. D. Rubin,<sup>35</sup> F. Sabatié,<sup>7</sup> C. Salgado,<sup>22</sup> J. P. Santoro,<sup>2,38</sup> V. Sapunenko,<sup>2</sup> R. A. Schumacher,<sup>4</sup> V. S. Serov,<sup>18</sup> Y. G. Sharabian,<sup>2</sup> D. Sharov,<sup>1</sup> J. Shaw,<sup>31</sup> E. S. Smith,<sup>2</sup> L. C. Smith,<sup>37</sup> D. I. Sober,<sup>5</sup> A. Stavinsky,<sup>18</sup> S. Stepanyan,<sup>2</sup> B. E. Stokes,<sup>12</sup> P. Stoler,<sup>25</sup> K. Stopani,<sup>1</sup> S. Strauch,<sup>33</sup> M. Taiuti,<sup>16</sup> S. Taylor,<sup>26</sup> D. J. Tedeschi,<sup>33</sup> R. Thompson,<sup>34</sup> A. Tkablazde,<sup>23,24</sup> S. Tkachenko,<sup>23,24</sup> L. Todor,<sup>4</sup> C. Tur,<sup>33</sup> M. Ungaro,<sup>29</sup> M. F. Vineyard,<sup>27,35</sup> A. V. Vlassov,<sup>18</sup> L. B. Weinstein,<sup>24</sup> D. P. Weygand,<sup>2</sup> M. Williams,<sup>4</sup> E. Wolin,<sup>2</sup> M. H. Wood,<sup>33</sup> A. Yegneswaran,<sup>2</sup> L. Zana,<sup>32</sup> and J. Zhang<sup>24</sup>

(CLAS Collaboration)

<sup>1</sup>Moscow State University, Skobeltsyn Nuclear Physics Institute and Physics Department, RU-119899 Moscow, Russia

<sup>2</sup>Thomas Jefferson National Accelerator Facility, Newport News, Virginia 23606, USA

<sup>3</sup>Arizona State University, Tempe, Arizona 85287, USA

<sup>4</sup>Carnegie Mellon University, Pittsburgh, Pennsylvania 15213, USA

<sup>5</sup>Catholic University of America, Washington, DC 20064, USA

<sup>6</sup>Christopher Newport University, Newport News, Virginia 23606, USA

<sup>7</sup>CEA-Saclay, Service de Physique Nucléaire, F-91191 Gif-sur-Yvette, Cedex, France

<sup>8</sup>College of William and Mary, Williamsburg, Virginia 23187, USA

<sup>9</sup>Edinburgh University, Edinburgh EH9 3JZ, United Kingdom

<sup>10</sup>Fairfield University, Fairfield, Connecticut 06824, USA

<sup>11</sup>Florida International University, Miami, Florida 33199, USA

<sup>12</sup>Florida State University, Tallahassee, Florida 32306, USA

<sup>13</sup>George Washington University, Washington, DC 20052, USA

<sup>14</sup>Idaho State University, Pocatello, Idaho 83209, USA

<sup>15</sup>Institut de Physique Nucleaire ORSAY, Orsay, France

<sup>16</sup>INFN, Sezione di Genova, I-16146 Genova, Italy

<sup>17</sup>INFN, Laboratori Nazionali di Frascati, I-00044 Frascati, Italy

<sup>18</sup>Institute of Theoretical and Experimental Physics, Moscow, RU-117259, Russia

<sup>19</sup>James Madison University, Harrisonburg, Virginia 22807, USA

<sup>20</sup>Kyungpook National University, Daegu 702-701, South Korea

<sup>21</sup>Massachusetts Institute of Technology, Cambridge, Massachusetts 02139, USA

<sup>22</sup>Norfolk State University, Norfolk, Virginia 23504, USA

<sup>23</sup>Ohio University, Athens, Ohio 45701, USA

<sup>24</sup>Old Dominion University, Norfolk, Virginia 23529, USA

<sup>25</sup>Rensselaer Polytechnic Institute, Troy, New York 12180, USA

<sup>26</sup>Rice University, Houston, Texas 77005, USA

<sup>27</sup>Union College, Schenectady, New York 12308, USA

<sup>28</sup>University of California at Los Angeles, Los Angeles, California 90095, USA

<sup>29</sup>*University of Connecticut, Storrs, Connecticut 06269, USA*<sup>30</sup>*University of Glasgow, Glasgow G12 8QQ, United Kingdom*<sup>31</sup>*University of Massachusetts, Amherst, Massachusetts 01003, USA*<sup>32</sup>*University of New Hampshire, Durham, New Hampshire 03824, USA*<sup>33</sup>*University of South Carolina, Columbia, South Carolina 29208, USA*<sup>34</sup>*University of Pittsburgh, Pittsburgh, Pennsylvania 15260, USA*<sup>35</sup>*University of Richmond, Richmond, Virginia 23173, USA*<sup>36</sup>*Universidad Tecnica Federico Santa Mara, Av. Espaa 1680 Casilla 110-V Valparaso, Chile*<sup>37</sup>*University of Virginia, Charlottesville, Virginia 22901, USA*<sup>38</sup>*Virginia Polytechnic Institute and State University, Blacksburg, Virginia 24061, USA*<sup>39</sup>*Yerevan Physics Institute, Yerevan 375036, Armenia*

(Received 10 September 2008; published 20 January 2009)

This paper reports on the most comprehensive data set obtained on differential and fully integrated cross sections for the process  $ep \rightarrow e' p \pi^+ \pi^-$ . The data were collected with the CLAS detector at Jefferson Laboratory. Measurements were carried out in the as yet unexplored kinematic region of photon virtuality  $0.2 < Q^2 < 0.6$  GeV<sup>2</sup> and invariant mass of the final hadron system  $W$  from 1.3 to 1.57 GeV. For the first time, nine independent one-fold differential cross sections were determined in each bin of  $W$  and  $Q^2$  covered by the measurements. A phenomenological analysis of the data allowed us to establish the most significant mechanisms contributing to the reaction. The nonresonant mechanisms account for a major part of cross sections. However, we find sensitivity to  $s$ -channel excitations of low-mass nucleon resonances, especially to the  $N(1440)P_{11}$  and  $N(1520)D_{13}$  states in kinematic dependencies of the one-fold differential cross sections.

DOI: [10.1103/PhysRevC.79.015204](https://doi.org/10.1103/PhysRevC.79.015204)

PACS number(s): 13.60.Le, 13.40.Gp, 14.20.Gk, 24.85.+p

## I. INTRODUCTION

An extensive research program is currently underway in Hall B at Thomas Jefferson National Accelerator Facility (Jefferson Lab) with the Continuous Electron Beam Accelerator Facility (CEBAF) large acceptance spectrometer (CLAS) detector, focused on studies of nucleon resonances ( $N^*$ ) in various exclusive channels of meson electroproduction off protons [1–3]. Part of this effort is aimed at the determination of electrocouplings for an entire spectrum of excited nucleon  $N^*$  and  $\Delta^*$  states versus the photon virtuality  $Q^2 = -(e - e')^2$ , where  $e$  and  $e'$  are the four-momentum vectors of the incoming and scattered electron, respectively. Comprehensive information on resonance electrocouplings and their evolution with  $Q^2$  is needed to probe the spatial and spin structure of the resonance transitions. This information is needed to enhance our understanding of the effective strong interaction that is at the core of internal baryon structure and the decay of baryons. It is also needed to firmly establish the connection of effective degrees of freedom such as (a) ‘constituent’ quarks in the binding potential or (b) ‘constituent’ quark scattering amplitudes to the elementary quarks and gauge gluons of QCD, the theory of the strong interaction.

In the past five years, single pseudoscalar meson electroproduction has been studied in several exclusive processes, e.g.,  $p\pi^0$ ,  $n\pi^+$ ,  $p\eta$ ,  $K\Lambda$ , and  $K\Sigma$  [4–18], which included differential cross sections with complete polar angle and azimuthal angle distributions, as well as several polarization observables. From these data sets, resonance transition electromagnetic form factors have been determined for the

$\Delta(1232)P_{33}$ ,  $N(1535)S_{11}$ , and  $N(1440)P_{11}$ , covering a wide range in  $Q^2$ .

Studies of charged double pion electroproduction off protons represent an important part at this effort. Single and double pion production are the two largest contributors to the total photo- and electroproduction cross sections off protons in the resonance region. The final states produced in these two exclusive channels have considerable hadronic interactions, or so-called final state interactions (FSI). FSI may be determined using the data of experiments with hadronic probes [19]. According to these data, the cross section for the  $\pi N \rightarrow \pi\pi N$  reaction has the second largest strength of all of the exclusive channels in the  $\pi N$  interaction. Considerable FSI between the  $\pi N$  and  $\pi\pi N$  final states result in substantial contributions to the amplitudes of both single and double pion electroproduction from the electroproduction amplitudes of the other channel. Accounting for these coupled-channel effects is essential in order to get the amplitude description compatible with the constraints imposed by unitarity. Therefore, for  $N^*$  studies both in single and double pion electroproduction, information is needed on the mechanisms contributing to each of these channels in order to properly take into account the impact from coupled-channel effects on the exclusive channel cross sections. The knowledge of single and double pion electroproduction mechanisms becomes even more important for  $N^*$  studies in channels with smaller cross sections such as  $p\eta$  or  $K\Lambda$  and  $K\Sigma$  production, as they could be significantly affected in leading order by coupled-channel effects produced by their hadronic interactions with the dominant single and double pion electroproduction channels. Therefore, comprehensive studies of single and double pion electroproduction are of key importance for the entire  $N^*$  research program.

\*deceased

The world data on double pion electroproduction in the nucleon resonance excitation region were rather scarce before the data from CLAS became available. Fully integrated cross sections for  $\pi\Delta$  isobar channels as a function of the invariant mass of the hadronic system  $W$  and photon virtualities  $Q^2$  were available from DESY [20]. However, the data are presented in very large kinematic bins,  $\Delta W = 200\text{--}300$  MeV and  $\Delta Q^2 = 0.2\text{--}0.6$  GeV<sup>2</sup>. Center-of-mass angular distributions for  $\pi^-$  were also measured but were averaged over a very large interval in  $Q^2$  from 0.3 to 1.4 GeV<sup>2</sup>. This makes it virtually impossible to determine the nucleon resonance parameters from such measurements.

The first detailed data on charged double pion electroproduction cross sections in the resonance region were obtained with CLAS [21,22]. The data were collected for  $W = 1.4\text{--}2.1$  GeV in 25 MeV bins and for  $Q^2 = 0.5\text{--}1.5$  GeV<sup>2</sup> in 0.3 GeV<sup>2</sup> wide bins. The current experiment covers invariant masses of  $\pi^-\pi^+$ ,  $\pi^+p$ , and  $\pi^-p$  in each  $(W, Q^2)$  bin for  $Q^2 = 0.2\text{--}0.6$  GeV<sup>2</sup> in 0.05 GeV<sup>2</sup> wide bins and for  $W = 1.30\text{--}1.57$  GeV with 25 MeV bins. In addition, angular distributions for  $\pi^-$ ,  $\pi^+$ , and proton, as well as angular distributions in  $\alpha_i$  ( $i = 1, 2, 3$ ) angles (see Sec. V for  $\alpha_i$  definitions), were measured. These very detailed measurements are crucial to determining the most significant production mechanisms for this process.

The CLAS data presented in this paper were collected with binning resolutions over  $W$  and  $Q^2$  surpassing by almost an order of magnitude what was achieved in previous measurements before the experiments with CLAS. These data analyzed together with the data on single pion electroproduction will allow us to extract the electrocoupling amplitudes of the  $N(1440)P_{11}$  and  $N(1520)D_{13}$  states. A certain advantage of the double pion channel is that the amplitudes of the  $N(1440)P_{11}$  resonance do not interfere with the high-mass tail of the  $\Delta(1232)P_{33}$  state, as is the case for the amplitudes in single  $\pi$  production.

The behavior of  $N^*$  electrocouplings at small photon virtualities is of particular interest. Studies of the magnetic transition form factor for the  $\Delta(1232)P_{33}$  in Ref. [23] revealed considerable meson-baryon dressing effects in addition to the three-quark core contributions. The dressing is expected to decrease with increasing  $Q^2$ . It is most pronounced at  $Q^2 < 1.0$  GeV<sup>2</sup> [24]. While the role of meson-baryon dressing effects has been studied based on the data on electrocouplings of the  $\Delta(1232)P_{33}$  state, for resonances heavier than the  $\Delta(1232)P_{33}$ , this remains an open question and is currently being addressed at Jefferson Lab through extensive theoretical efforts [24–27]. Accounting for these effects is a necessary step in probing quark and possibly gluonic degrees of freedom in baryons. The comparison of constituent quark model predictions [28–30] with the measured  $N^*$  electrocouplings [2,3], as well as the coupled-channels analysis of the data on reactions with hadronic probes [24], suggests considerable meson-baryon dressing effects at  $Q^2 < 0.5$  GeV<sup>2</sup> for the  $N(1440)P_{11}$  and  $N(1520)D_{13}$  electrocouplings. Therefore, the information on these states at low photon virtualities from charged double pion electroproduction may further elucidate the relevant degrees of freedom in resonance excitation at hadronic distance scales.

The data presented in this paper can also provide information on the  $p \rightarrow \Delta$  axial transition form factor. Current algebra [31] relates the contact term in the set of nonresonant Born terms for  $\pi\Delta$  isobar channels to the axial transition form factors. These contact terms could be fit to the data within the framework of the JM approach [32,33]. So far, the  $p \rightarrow \Delta$  axial transition form factor has been determined mostly from neutrino-induced reactions [34–36]. Axial transition form factors offer a complementary view of baryon structure, seen in the axial vector currents, while electroproduction experiments usually access baryon structure through vector currents. This will be the subject of a forthcoming paper. Recently, lattice QCD results have become available [37], which make the experimental study of the nucleon axial structure an important topic of hadronic physics.

## II. ANALYSIS TOOLS

The presence of three hadrons in the final state presents considerable complications in the phenomenological analysis. Efforts to apply partial wave analysis (PWA) techniques to double pion production by electromagnetic probes are limited to photoproduction, where very high statistics data are available [38,39]. A strong reduction in statistics for individual bins in  $Q^2$  makes application of PWA methods in double pion electroproduction data much more difficult. Moreover, there is no model-independent way to disentangle resonant and nonresonant mechanisms in any given partial wave. Therefore, reaction models are needed to isolate the resonant parts in the double pion production amplitudes and evaluate the  $N^*$  electromagnetic transition form factors.

Following the pioneering effort of Ref. [40], several approaches have been developed more recently for the description of double pion photo- and electroproduction in the resonance region [41–47]. These efforts were based on a very limited amount of experimental data: mostly on  $W$  and  $Q^2$  dependencies for fully integrated cross sections and on invariant mass distributions for various pairs of the final state hadrons. The reaction models used meson-baryon degrees of freedom:  $N$ ,  $\Delta$ ,  $\pi$ ,  $\sigma$ , and  $\rho$ . Effective meson-baryon Lagrangian operators were constructed based on Lorentz invariance, gauge invariance, and crossing symmetry. For the description of experimental data, a limited set of nonresonant meson-baryon diagrams was used with amplitudes calculated from effective Lagrangians together with contributions from several, mostly low-lying nucleon resonances ( $M < 1.6$  GeV). A general framework for the implementation of other meson-baryon degrees of freedom was proposed in Ref. [44], but so-far has not been fully realized.

The meson-baryon diagrams in reaction models may account for many partial waves. However, in any reaction model, we need to truncate the infinite set of meson-baryon diagrams, keeping just the relevant mechanisms. Moreover, the choice of a particular effective Lagrangian, describing meson-baryon interactions, may be done only at a phenomenological level.

At the distance scale appropriate for the size of hadrons, the amplitudes of effective meson-baryon interactions contributing to the reaction cannot be expanded over a small parameter

except for a small kinematic region near threshold  $W$  and  $Q^2 < 0.2 \text{ GeV}^2$  accessible for chiral perturbation theory. This feature makes it impossible to select contributing diagrams based on a perturbative expansion for the entire double pion reaction phase space covered by the CLAS measurements. So far, no approach has been developed based on a fundamental theory that would allow either a description of an effective Lagrangian or a selection of the contributing meson-baryon mechanisms from basic principles. We therefore have to rely on fits to the now available detailed experimental data sets to develop reaction models that contain the relevant mechanisms.

The large reaction phase-space coverage of CLAS data opens up qualitatively new opportunities for the analysis of charged double pion electroproduction. The exclusive channel  $ep \rightarrow e' p \pi^+ \pi^-$  offers many observables for the analysis. The hadronic final state can be projected on nine independent one-fold differential cross sections in each  $W$  and  $Q^2$  bin. For the first time, all of these observables are experimentally accessible [21,48]. By studying the kinematic dependencies of the differential cross section and their correlations, we are able to establish the presence and strength of the relevant reaction mechanisms. A phenomenological approach [32,33,49–55] was developed in a collaboration between Jefferson Lab and Moscow State University, referred to herein as “JM”. This approach is intended to establish all significant mechanisms seen in the observables of charged double pion electroproduction, to isolate the resonant parts of the amplitudes, and to derive the electrocouplings of nucleon resonance transitions from fits of all measured observables combined.

### III. EXPERIMENT

The measurement was carried out using the CLAS detector [56] at the Jefferson Lab. CLAS provides almost complete

angular coverage in the center-of-mass frame. It is well suited for conducting experiments that require detection of two or more particles in the final state. Such a detector and the continuous beam produced by CEBAF provide excellent conditions for measuring the  $ep \rightarrow e' p' \pi^+ \pi^-$  cross section by detecting the outgoing electron, proton, and at least one pion in coincidence.

#### A. Apparatus

The main magnetic field of CLAS is provided by six superconducting coils, symmetrically arranged around the beamline, which generate an approximately toroidal field in the azimuthal direction around the beam axis. The gaps between the coil cryostat are instrumented with six identical detector packages, referred to here as “sectors,” as shown in Fig. 1. Each sector consists of three regions (region 1, region 2, and region 3) of drift chambers (DCs) [57] to determine the trajectories of the charged particles as they travel from the target outward in the magnetic field, a Cherenkov counter (CC) [58] for electron identification, scintillator counters (SCs) [59] for charged particle identification using the time-of-flight (TOF) method, and an electromagnetic calorimeter (EC) [60] for electron identification. The liquid-hydrogen target was located in the center of the detector. To reduce the electromagnetic background resulting from Møller scattering off atomic electrons, a second smaller normal-conducting toroidal magnet (mini-torus) was placed symmetrically around the target. This additional magnetic field prevented Møller electrons from reaching the sensitive detector volume. A totally absorbing Faraday cup, located at the very end of the beamline, was used to determine the integrated beam charge passing through the target. The CLAS detector provides  $\approx 80\%$  of  $4\pi$  solid-angle coverage. The efficiency of detection

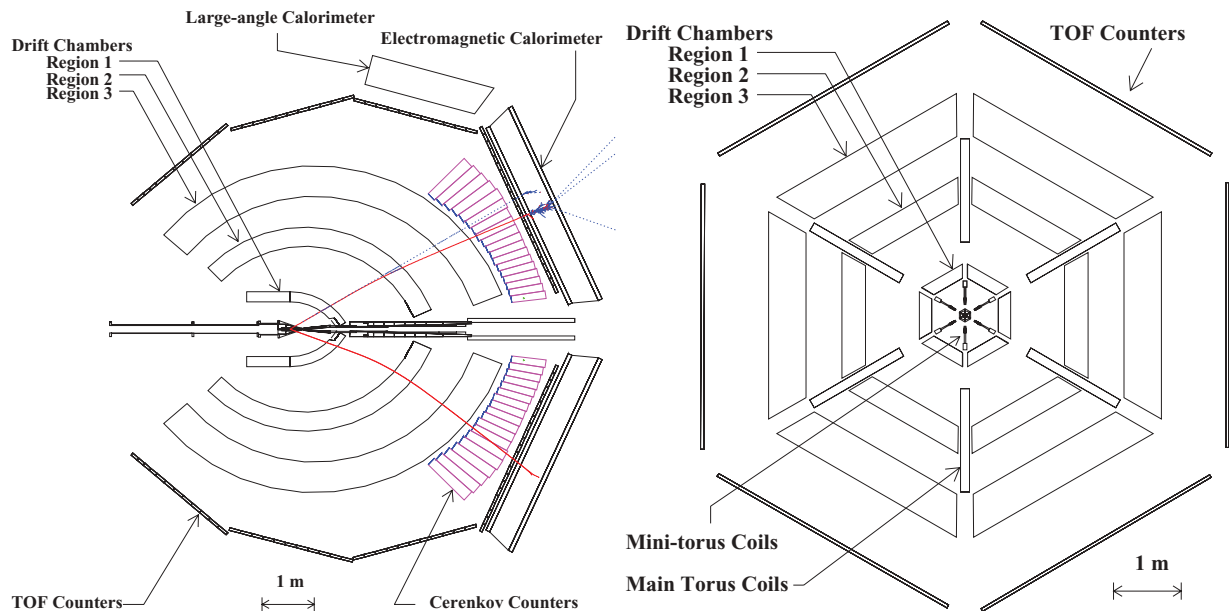


FIG. 1. (Color online) Cross-sectional views of the CLAS detector. The left panel shows a cut along the beamline and through the midplane of two opposite sectors. The right panel shows a cut perpendicular to the beamline and through the nominal target center. Descriptions of the detector elements are given in the text of Sec. III A.

and reconstruction for single stable charged particles in the fiducial regions of CLAS is greater than 95%. The combined information from tracking in the DC and the SC systems allows us to reliably separate protons from positive pions. Additional constraints for event selection come from the overdetermined kinematics, which allows use of the missing mass technique.

Due to possible slight misalignments in the DC positions and small inaccuracies in the description of the torus magnetic field, the reconstructed momentum and angle of particles may have small systematic deviations from the physical value. To correct these deviations, elastic electron-proton scattering was checked and the electron three-momenta were corrected to ensure the proper mass peak position for the recoil proton [61]. The proton energy losses in CLAS were estimated from a simulation of proton propagation through the detector materials in kinematics corresponding to charged double pion electroproduction.

### B. Data taking and data reduction

This analysis is based on data taken during the 1999 e1c run period. The 1.515 GeV electron beam at a current of 3 nA was incident on a 5-cm-long liquid-hydrogen target corresponding to an instantaneous luminosity of  $\sim 4 \times 10^{33} \text{ cm}^{-2} \text{ s}^{-1}$ . The size of the beam spot at the target was  $\sim 0.2$  mm, with position fluctuations  $< \pm 0.04$  mm. The main torus current was set at 1500 A, which created a magnetic field of about 0.8 T at polar angles of  $20^\circ$  that decreased with increasing polar angle. The CLAS event readout was triggered by a coincidence of signals from an electromagnetic calorimeter module and a threshold gas Cherenkov counter in one of the six sectors, generating a total event rate of  $\sim 2$  kHz. The number of accumulated triggers at these detector settings was about  $4.2 \times 10^8$ . These data were further analyzed to extract the differential cross sections for the  $ep \rightarrow e'p'\pi^+\pi^-$  reaction.

### IV. EVENT SELECTION

The  $ep \rightarrow e'p'\pi^+\pi^-$  reaction is selected by measuring the scattered electron, as well as the proton and  $\pi^+$  in the hadronic final state. In the magnetic field configuration used in this measurement, the negatively charged pions have a smaller probability for detection than the positively charged particles. However, the process is kinematically overconstrained, and the detection of all particles in the final state is not required for an unambiguous identification of the exclusive reaction. To retain maximum acceptance, we chose to not require detection of the  $\pi^-$ , but rather infer the presence and kinematics of the undetected  $\pi^-$  by computing the mass of the undetected particle from four-momentum conservation and its charge from charge conservation. The two other topologies, with either undetected proton or undetected  $\pi^+$ , have considerably lower rates and were used for systematics studies and for cross-checks, but are not included in the determination of the final cross sections.

For each event, we identify as the electron candidate the first coming negatively charged particle detected in the electromagnetic calorimeter and the Cherenkov counter. To

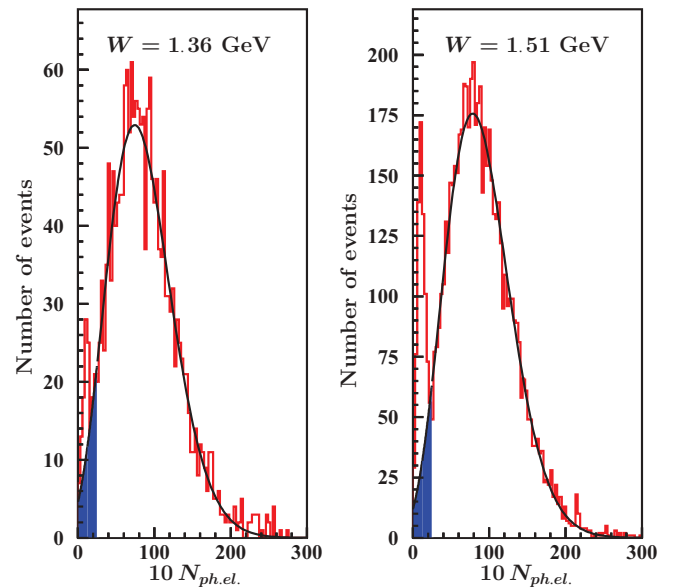


FIG. 2. (Color online) Distribution of photoelectrons in the Cherenkov counter for  $0.3 < Q^2 < 0.4 \text{ GeV}^2$  in two  $W$  bins centered at the values shown in each plot. The curves represent a Poisson fit.

select true electrons, we apply a cut in the number of photoelectrons ( $N_{\text{phe}} \geq 2.5$ ) produced by the Cherenkov light signal in the photomultipliers. This cut also eliminates a small fraction of electrons ( $< 6\%$ ), as shown in Fig. 2. The shadowed areas correspond to the cut-out electrons. A special procedure was developed to account for these electrons in the evaluation of the reconstruction efficiency, based on the extrapolation of the photoelectron spectra into the cut-out areas using a fit based on a Poisson distribution. The quality of electron identification may be seen in Fig. 3, where we display the energies deposited in the outer part of the calorimeter versus the energies deposited in the inner part of the EC, normalized to the momenta of the incoming particles. A spot from minimum-ionizing pions, clearly seen in inclusive electron events (top part of Fig. 3), disappears after applying the described cuts for electron selection (bottom part of Fig. 3).

Using information from the time-of-flight scintillators and the path length determined by tracking, the particle's velocity  $\beta$  was determined. The information from the drift chambers, combined with the known magnetic field, provides a measurement of the particle momentum  $p$ . Relativistic relations between particle mass, momentum, and velocity were used to determine the particle's mass, allowing us to separate pions, kaons, and protons in the kinematic range covered by the measurement. Figure 4 shows the velocity versus the momentum for positively charged particles.

After identification of the three particles, events were selected with one electron, one proton, and one  $\pi^+$ . The squared missing mass distribution is shown in Fig. 5, which clearly shows the pion mass peak and also indicates that multi-pion background ( $> 2\pi$ ) contributes less than 1% to the total number of charged double pion events selected by the cuts. The small background is related to the kinematic coverage of our experiment  $W < 1.57 \text{ GeV}$ , where the exclusive channels

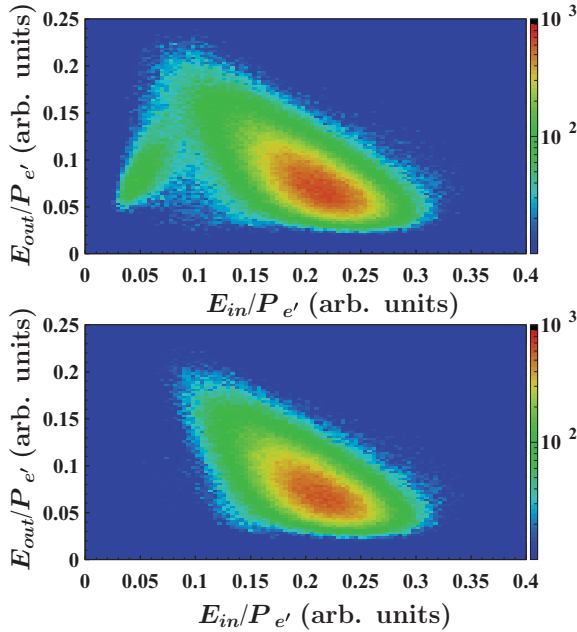


FIG. 3. (Color online) Distributions for the energies deposited in the outer part ( $E_{\text{out}}$ ) vs the energies deposited in the inner part ( $E_{\text{in}}$ ) of the EC normalized to the momenta of the outgoing particles ( $P_{e'}$ ). The distribution for the accumulated triggers is shown in the top plot, while the distribution for the events selected, applying the photoelectron cut, is shown in the bottom plot.

with more than two pions in the final state are suppressed due to their thresholds. The almost negligible contribution from the multi-pion background and the rather small radiative effects (see Sec. V F) allowed us to apply a wide exclusivity cut over the squared missing mass distribution, shown in Fig. 5 by the two arrows, in order to collect the majority of the  $2\pi$  events.

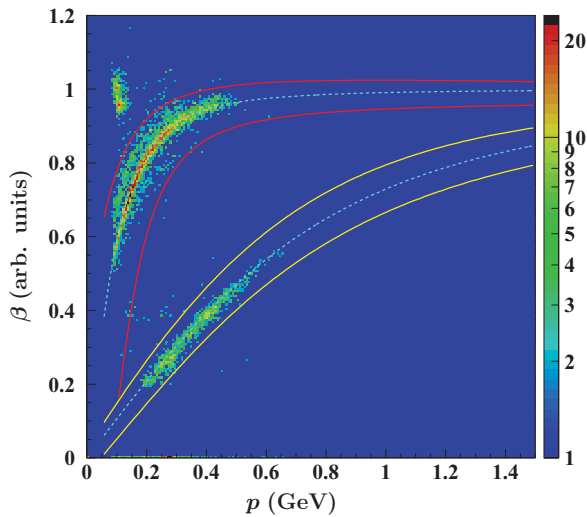


FIG. 4. (Color online)  $\beta$  vs momentum for positively charged hadrons; solid curves show the cuts used to identify pions and protons; dashed curves show the explicit  $\beta$  vs  $p$  relationships, using the pion and proton mass, respectively. The events near  $\beta = 1$  and  $p = 0.1$  GeV are positrons, e.g., from  $\pi^0$  Dalitz decay. The data were collected in a single scintillator bar.

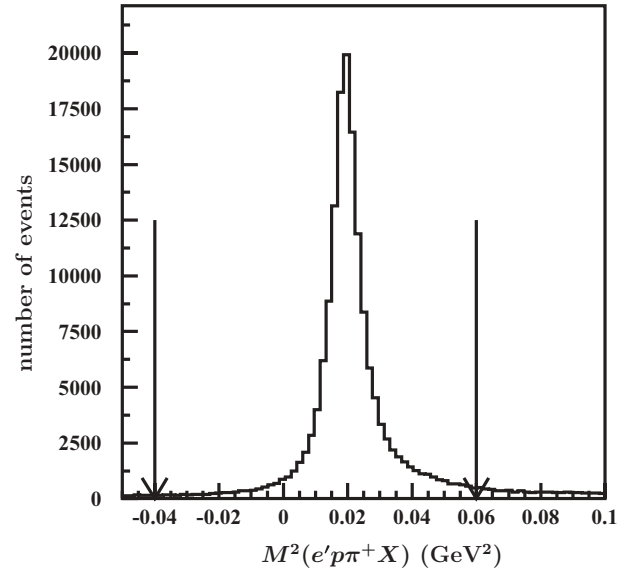


FIG. 5. Distribution of squared missing mass  $M^2(e' p\pi^+ X)$  ( $\text{GeV}^2$ ). The arrows show the exclusivity cut.

The CLAS detector has an active detection solid angle smaller than  $4\pi$  due to the space filled with the torus magnet coils. The angles covered by the torus magnet coils are not equipped with any detection system and therefore give rise to inactive areas. The boundaries of the active areas are not well defined and do not provide regions for particle reconstruction with full reconstruction efficiency. Therefore, for the analysis, we accept only events inside specific fiducial areas whose contours are defined by parametrizations of the kinematic variables of each particle. Within these well-defined regions, acceptances and track reconstruction efficiencies are well understood using Monte Carlo simulations.

After all selections have been applied, there remain about 130 000 exclusive  $p\pi^+\pi^-$  events. Figure 6 shows the  $Q^2$  vs  $W$  distribution for the selected  $2\pi$  events.

## V. CHARGED DOUBLE PION ELECTROPRODUCTION CROSS SECTIONS

The kinematics of the three-body  $p\pi^+\pi^-$  final state are unambiguously determined by five independent variables [62]. However, the choice of these variables is not unique. In this section, we specify the kinematic variables we employ to describe the  $p\pi^+\pi^-$  final state and related phase-space element for the five-fold differential cross section. Note that the double pion cross sections for virtual photon absorption are five-fold differential, while the double pion electroproduction cross sections are seven-fold differential, since they contain the additional variables  $W$  and  $Q^2$ . Then we describe the procedure to evaluate the five-fold differential charged double pion cross section from experimental data from the seven-dimensional event distributions. The five-fold differential cross section contains complete information on double pion production at fixed  $Q^2$  and  $W$ . However, the limited statistics do not allow direct study of the five-fold differential cross sections. Therefore, for the physics analysis, we use various

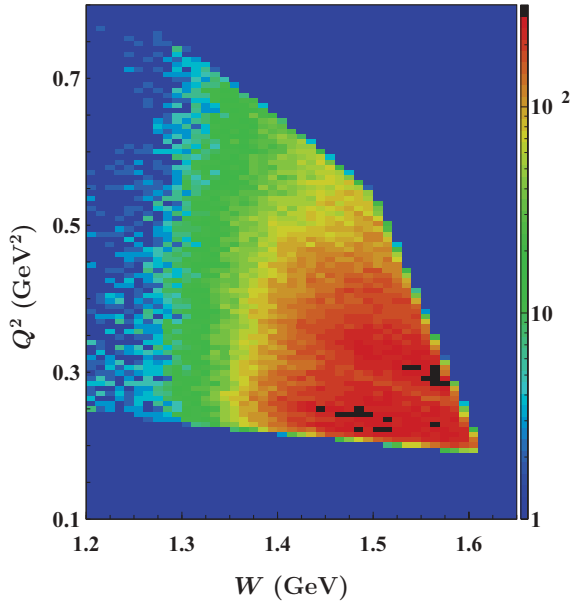


FIG. 6. (Color online)  $Q^2$  ( $\text{GeV}^2$ ) vs  $W$  ( $\text{GeV}$ ) distribution for the selected  $2\pi$  events. The grid shows the binning used for the evaluation of the cross section. Only cells inside the allowed phase space were used for that purpose.

one-fold differential cross sections, obtained by integrating the five-fold differential cross section over the four other variables.

### A. Kinematic variables

We adopt the following set of variables to describe the three-body final state: invariant mass of the first pair of particles  $M_{12}$ , invariant mass of the second pair of particles  $M_{23}$ , the first particle solid angle  $\Omega$ , and the angle between two planes: plane A is defined by the three-momenta of the virtual photon and the first hadron, and plane B is defined by the three-momenta of the two other hadrons (see Fig. 7).

We use three different assignments for the first, second, and third final state hadrons:

- (i) Invariant mass of the  $p\pi^+$  pair, invariant mass of the  $\pi^+\pi^-$  pair, the final proton spherical angles  $\theta_p$  and  $\varphi_p$ , and the angle  $\alpha_{(pp')(\pi^+\pi^-)}$  between the two planes: B, composed of the momenta of the  $\pi^+\pi^-$  pair; and A, composed of the momenta of the initial and final protons (choice 1).
- (ii) Invariant mass of the  $\pi^+\pi^-$  pair, invariant mass of the  $p\pi^+$  pair,  $\pi^-$  spherical angles  $\theta_{\pi^-}$  and  $\varphi_{\pi^-}$ , and the angle  $\alpha_{(p\pi^-)(p'\pi^+)}$  between the two planes: B, composed of the momenta of the final state proton  $p'$  and  $\pi^+$ ; and A, composed of the initial state proton  $p$  and  $\pi^-$  (choice 2).
- (iii) Invariant mass of the  $p\pi^+$  pair, invariant mass of the  $p\pi^-$  pair,  $\pi^+$  spherical angles  $\theta_{\pi^+}$  and  $\varphi_{\pi^+}$ , and the angle  $\alpha_{(p\pi^+)(p'\pi^-)}$  between the two planes: B, composed of the momenta of the final state proton  $p'$  and  $\pi^-$  and A, composed of the initial state proton  $p$  and  $\pi^+$  (choice 3).

The five-fold differential cross sections were obtained for all three sets of variables. The emission angles for the final particles in the second set of variables are shown in Fig. 7. For the other sets, the emission angles are defined in a similar way. In the physics analysis, described in Sec. VI, the second set of variables is used. These variables are suitable for the description of charged double pion electroproduction through a  $\pi^-\Delta^{++}$  intermediate state, which represents the main contributor of all isobar channels in the kinematic area covered by our data. The relations between the four-momenta of the final state hadrons and the kinematic variables may be found in the Appendix.

### B. Evaluation of charged double pion cross sections

The selected double  $\pi$  events were collected in seven-dimensional cells, composed of  $W$ ,  $Q^2$ , invariant masses of the first pair  $M_{12}$  and the second pair  $M_{23}$  of the final state particles, solid angle for the first final state particle, and the angle  $\alpha_i$  between planes A and B. The cross sections were determined

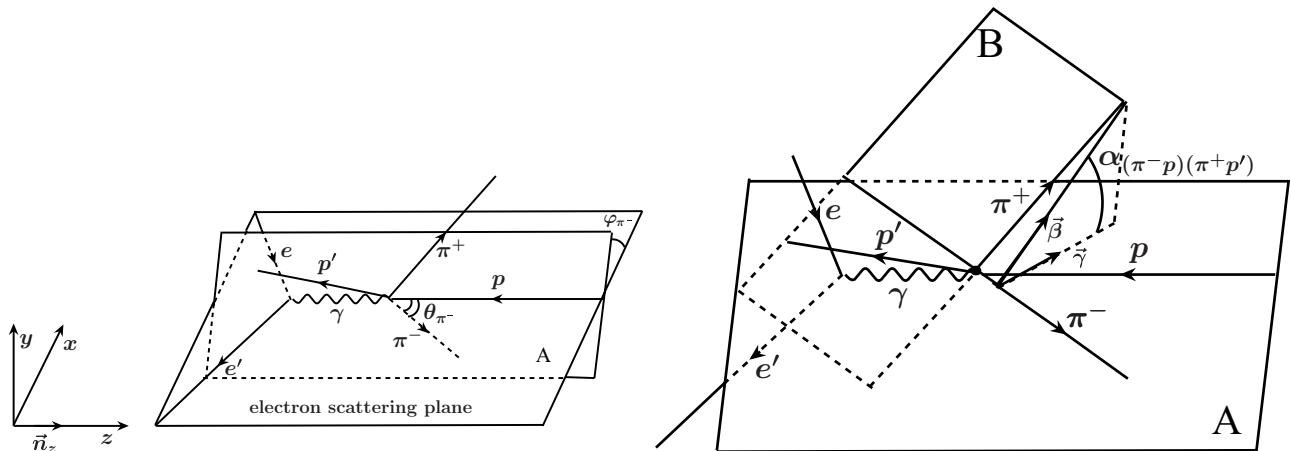


FIG. 7. Kinematic variables for the  $ep \rightarrow e'p'\pi^+\pi^-$  reaction (choice 2 in Sec. V A). The left plot shows the  $\pi^-$  spherical angles  $\theta_{\pi^-}$  and  $\varphi_{\pi^-}$ , while the right plot shows the angle  $\alpha_{(\pi^-p)(\pi^+p')}$  of the plane defined by the momenta of the final  $p\pi^+$  pair with respect to the plane comprised by the momenta of the initial proton  $p$  and  $\pi^-$ .

only for those  $W$  cells that were fully inside the kinematically allowed area. Special procedures were developed to evaluate the one-fold differential cross sections for the final state particle invariant mass values near edges of the reaction phase space (see Sec. [VD,VE](#)). All frame-dependent variables and the cross sections were evaluated in the center-of-mass frame.

For the second choice of kinematic variables, the seven-fold differential cross sections  $\frac{d\sigma}{dW dQ^2 d^5\tau_2}$ , where  $d^5\tau_2 = dM_{p\pi^+} dM_{\pi^+\pi^-} d\Omega_{\pi^-} d\alpha_{(p\pi^-)(p'\pi^+)}$ , are given by the number of  $p\pi^+\pi^-$  events  $\Delta N$  and efficiencies  $\epsilon$  in the seven-dimensional cells as

$$\frac{d\sigma}{dW dQ^2 d^5\tau_2} = \frac{1}{\epsilon \epsilon_{\text{ch}} R} \frac{\Delta N}{\Delta W \Delta Q^2 \Delta^5\tau_2 L}. \quad (1)$$

The number of events inside the seven-dimensional cells were corrected for contamination from the target walls, which was measured in separate runs with an empty target cell. The efficiency  $\epsilon$  in any seven-dimensional cell was determined in detailed Monte Carlo simulations. The inactive zones of CLAS and all cuts on phase space used in the event selection were included in the efficiency evaluation. The factor  $\epsilon_{\text{ch}}$  accounts for the Cherenkov counter efficiency, which was determined separately.  $R$  accounts for radiative corrections. The integrated luminosity  $L$  was determined from the total beam charge  $Q$  measured in the Faraday cup, combined with the information on target length and target density:

$$L = Q \frac{l_t D_t N_A}{q_e M_H}, \quad (2)$$

where  $q_e$  is the elementary charge,  $D_t$  is the density of hydrogen ( $D_t = 0.073$  g/cm<sup>3</sup>),  $l_t$  is the length of the target ( $l_t = 5$  cm),  $M_H$  is the molar density of hydrogen ( $M_H = 1$  g/mol), and  $N_A$  is Avogadro's number. The luminosity value was verified by reproducing elastic  $ep$  cross sections with the same data set. A comparison of the elastic  $ep$  scattering cross sections determined from our data with a parametrization of world data given in Ref. [\[63\]](#) showed agreement within better than 5%.  $\Delta W$  and  $\Delta Q^2$  are bins over  $W$  and  $Q^2$ , and  $\Delta^5\tau_2$  represents the element of hadronic five-dimensional phase space for the second choice of kinematic variables:

$$\Delta^5\tau_2 = \Delta M_{p\pi^+} \Delta M_{\pi^+\pi^-} \Delta \cos(\theta_{\pi^-}) \Delta \varphi_{\pi^-} \Delta \alpha_{(p\pi^-)(p'\pi^+)}. \quad (3)$$

The seven-fold differential cross sections for the other two choices of kinematic variables listed in Sec. [VA](#) may be obtained from Eq. [\(3\)](#), by substituting the phase-space element  $\Delta^5\tau_2$  with

$$\Delta^5\tau_1 = \Delta M_{p\pi^+} \Delta M_{\pi^+\pi^-} \Delta \cos(\theta_p) \Delta \varphi_p \Delta \alpha_{(pp')(\pi^-\pi^+)}, \quad (4)$$

$$\Delta^5\tau_3 = \Delta M_{p\pi^-} \Delta M_{p\pi^+} \Delta \cos(\theta_{\pi^+}) \Delta \varphi_{\pi^+} \Delta \alpha_{(p\pi^+)(p'\pi^-)}.$$

In the single photon exchange approximation, the seven-fold differential electron scattering cross section is related to the hadronic five-fold differential cross section as [\[64\]](#)

$$\begin{aligned} & \frac{d\sigma}{dM_{p\pi^+} dM_{\pi^+\pi^-} d\Omega_{\pi^-} d\alpha_{(p\pi^-)(p'\pi^+)}} \\ &= \frac{1}{\Gamma_\nu} \frac{d\sigma}{dW dQ^2 dM_{p\pi^+} dM_{\pi^+\pi^-} d\Omega_{\pi^-} d\alpha_{(p\pi^-)(p'\pi^+)}} \end{aligned}, \quad (5)$$

where  $\Gamma_\nu$  is virtual photon flux, given by

$$\Gamma_\nu = \frac{\alpha}{4\pi} \frac{1}{E_b^2 M_p^2} \frac{W(W^2 - M_p^2)}{(1 - \epsilon)Q^2}, \quad (6)$$

and  $\alpha$  is the fine structure constant,  $E_b$  is the beam energy,  $M_p$  is the proton mass, and  $\epsilon$  is the virtual photon transverse polarization given by

$$\epsilon = \left[ 1 + 2 \left( 1 + \frac{\nu^2}{Q^2} \right) \tan^2 \left( \frac{\theta_e}{2} \right) \right]^{-1}, \quad (7)$$

where  $\nu$  is the virtual photon energy, and  $\theta_e$  is the electron scattering angle in the laboratory frame.  $W$ ,  $Q^2$ , and  $\theta_e$  were taken at their respective bin centers.

The limited statistics do not allow use of correlated multi-fold differential cross sections for physics analysis. In the physics analysis, we instead used one-fold differential cross sections, obtained after integration of the five-fold differential cross sections over four kinematic variables. The number of five-dimensional bins contributing to the individual bins of the one-fold differential cross sections range from 375 at  $W = 1.31$  GeV to 1600 at  $W > 1.38$  GeV. Summing up events in all five-dimensional bins, reasonable statistical accuracy is achieved for the one-fold differential cross sections (see Figs. [9, 13, 14, 20, 21](#)). We obtained in each  $(W, Q^2)$  bin covered by measurements a set of nine one-fold differential cross sections, consisting of  $\pi^+\pi^-$ ,  $p\pi^+$ , and  $p\pi^-$  mass distributions,  $\theta_i$  angular distributions, as well as three distributions over angles  $\alpha_i$  ( $i = 1, 2, 3$ ), where the index  $i$  stands for the  $i$ th set of kinematic variables, defined in the Sec. [VA](#). These one-fold differential cross sections represent the integrals from the five-fold differential cross section over four variables as

$$\begin{aligned} \frac{d\sigma}{dM_{\pi^+\pi^-}} &= \int \frac{d^5\sigma}{d^5\tau_2} d^4\tau_{\pi^+\pi^-}, \\ d^4\tau_{\pi^+\pi^-} &= dM_{\pi^-p} d\Omega_{\pi^-} d\alpha_{(p\pi^-)(p'\pi^+)}; \\ \frac{d\sigma}{dM_{\pi^+p}} &= \int \frac{d^5\sigma}{d^5\tau_2} d^4\tau_{\pi^+p}, \\ d^4\tau_{\pi^+p} &= dM_{\pi^+\pi^-} d\Omega_{\pi^-} d\alpha_{(p\pi^-)(p'\pi^+)}; \\ \frac{d\sigma}{dM_{\pi^-p}} &= \int \frac{d^5\sigma}{d^5\tau_3} d^4\tau_{\pi^-p}, \\ d^4\tau_{\pi^-p} &= dM_{\pi^+\pi^-} d\Omega_{\pi^+} d\alpha_{(p\pi^+)(p'\pi^-)}; \\ \frac{d\sigma}{d(-\cos\theta_i)} &= \int \frac{d^5\sigma}{d^5\tau_i} d^4\tau_i, \\ d^4\tau_i &= dM_{\pi^+\pi^-} dM_{\pi^+p} d\varphi_i d\alpha_i; \\ \frac{d\sigma}{d(\alpha_i)} &= \int \frac{d^5\sigma}{d^5\tau_i} d^4\tau_i, \\ d^4\tau_i &= dM_{\pi^+\pi^-} dM_{\pi^+p} d\Omega_i. \end{aligned} \quad (8)$$

In the actual cross section calculations, the integrals in Eq. [\(8\)](#) were substituted by the respective sums over the five-dimensional kinematic bins for the hadronic cross sections.

All cross sections represent independent one-dimensional projections of the five-fold differential cross sections. Any of the nine one-fold differential cross sections provides



independent information and cannot be computed from the eight remaining projections.

### C. Interpolation of five-fold differential cross section into the CLAS detector areas of zero acceptance

As discussed in Sec. IV, the CLAS detector has areas with zero acceptance. The contributions from the five-fold differential cross sections in such areas must be taken into account to obtain the integrated one-fold differential cross sections. We developed a special procedure to extend the five-fold differential cross sections in the areas of CLAS with zero acceptance.

We used the general  $\varphi_i$  ( $i = 1, 2, 3$ ) dependence of the five-fold differential cross sections fixing the other four kinematic variables:

$$\frac{d^5\sigma}{d^5\tau_i} = A + B \cos 2\varphi_i + C \cos \varphi_i + B' \sin 2\varphi_i + C' \sin \varphi_i. \quad (9)$$

The first three terms are valid for any exclusive channel and for any kind of particular reaction dynamics, being a consequence of rotational invariance of the production amplitudes. The last two terms appear in the five-fold differential cross sections for three-body final states. After integration over the  $\alpha_i$  angles, these two terms vanish as a consequence of parity conservation. The statistics in the populated bins is too small to allow evaluation of the  $A, B, C, B'$ , and  $C'$  coefficients from the data in the populated bins alone. Hence, we used both data and input from the models fit to the data to evaluate these coefficients. The coefficient ratios  $R_j$  ( $R_1 = B/A$ ,  $R_2 = C/A$ ,  $R_3 = B'/A$ ,  $R_4 = C'/A$ ) were taken from phenomenological models for charged double pion electroproduction fit to our data. The coefficient  $A$  was determined from the data on the five-fold differential cross sections in the populated five-dimensional bins  $\frac{d\sigma_{\text{meas}}}{dM_{p\pi^+} dM_{\pi^+\pi^-} d\Omega d\alpha_{(p\pi^-)(p'\pi^+)}}$  as

$$\begin{aligned} & \sum_{\Delta\varphi_{\pi^-}} \frac{d\sigma_{\text{meas}}}{dM_{p\pi^+} dM_{\pi^+\pi^-} d\Omega d\alpha_{(p\pi^-)(p'\pi^+)}} \Delta\varphi \\ &= A(2\pi - \Delta\tilde{\varphi}) - R_1 A \int_{\Delta\tilde{\varphi}} \cos(2\varphi_{\pi^-}) d\varphi_{\pi^-} \\ & \quad - R_2 A \int_{\Delta\tilde{\varphi}} \cos(\varphi_{\pi^-}) d\varphi_{\pi^-} - R_3 A \int_{\Delta\tilde{\varphi}} \sin(2\varphi_{\pi^-}) d\varphi_{\pi^-} \\ & \quad - R_4 A \int_{\Delta\tilde{\varphi}} \sin(\varphi_{\pi^-}) d\varphi_{\pi^-}, \end{aligned} \quad (10)$$

where the sum is running over the populated five-dimensional bins, while the integrals are taken over the CLAS areas of zero acceptance  $\Delta\tilde{\varphi}$ . The five-fold differential cross sections in the CLAS areas of zero acceptance were estimated from Eq. (9) with coefficients  $A, B, C, B', C'$  calculated from Eq. (10).

To determine the ratios  $R_j$  within the framework of the phenomenological models, we propagated the five-fold differential cross sections into the CLAS areas of zero acceptance, using the JM03 model predictions for the shape of the five-fold

differential cross sections [49–51]. The parameters of the JM03 model were determined from previous CLAS charged double pion data in the resonance region [21]. In this way preliminary estimates for the one-fold differential cross sections were obtained. Similar approaches to propagating the five-fold differential cross sections into the CLAS areas of zero acceptance were used in previous charged double pion data analyses, published in Refs. [21,65]. In the next step, the parameters of JM03 were further adjusted to reproduce preliminary estimates of the one-fold differential cross sections. The  $R_j$  coefficients were calculated within the framework of the JM03 approach after mentioned adjustment of the JM03 parameters. The coefficients  $A$  for the  $\varphi$  independent parts of the five-fold differential cross sections [see Eq. (9)] were obtained from the data in the populated bins, according to Eq. (10), using the improved estimates for  $R_j$ . Finally, the one-fold differential charged double pion cross sections were obtained as described in Sec. VB, using the five-fold differential cross sections in the CLAS areas of zero acceptance determined from Eq. (9) with values of  $A, B, C, B'$ , and  $C'$  determined as described above.

Since the model was used to evaluate the ratios  $R_j$ , the model assumptions affect mostly the  $\varphi$ -dependent parts in Eq. (9). After integration over  $\varphi_i$  angles, these parts disappear. Nevertheless, as follows from Eq. (10), the model assumptions used to interpolate the charged double pion cross sections into the CLAS areas of zero acceptance will increase the uncertainties of the one-fold differential cross sections obtained in our analysis. Detailed studies to evaluate these uncertainties were carried out and are described below.

First, we estimated the overall contribution from the inefficient areas to the one-fold differential cross sections, calculating them in two ways: (1) by including the contributions from the areas of zero acceptance in CLAS, as described above, and (2) by excluding them. In all cases, the two sets of values were found to overlap well inside the statistical uncertainties in the entire kinematic region covered in the experiment. One example is shown in Fig. 9.

In Fig. 8 we show a comparison of the fully integrated charged double pion cross sections. Again, within the entire kinematic area the differences between the two sets of cross sections are well within the statistical uncertainties.

In the next step, we investigate how the one-fold differential cross sections may be affected by the model assumptions used in the procedure described above. Since only  $\varphi$ -independent parts of Eq. (9) contribute to the one-fold differential cross sections, we need to know the model uncertainties just for the  $A$  coefficients. As follows from Eq. (9), the influence of the  $\varphi$ -dependent parts on the  $A$  coefficients depend on (a) the relative contributions of the  $\varphi$ -dependent parts to the five-fold differential cross sections and (b) the ratio  $\Delta\tilde{\varphi}/2\pi$ , where  $\Delta\tilde{\varphi}$  is the overall  $\varphi$  coverage of the CLAS areas of zero acceptance. The relative contributions from the  $\varphi$ -dependent parts is estimated by fitting the  $\varphi_i$  angular distributions,<sup>1</sup> using Eq. (9) with  $A, B$ , and  $C$  coefficients as free parameters.

<sup>1</sup> $i = 1, 2, 3$  and stands for the set of kinematic variables, defined in Sec. VA.

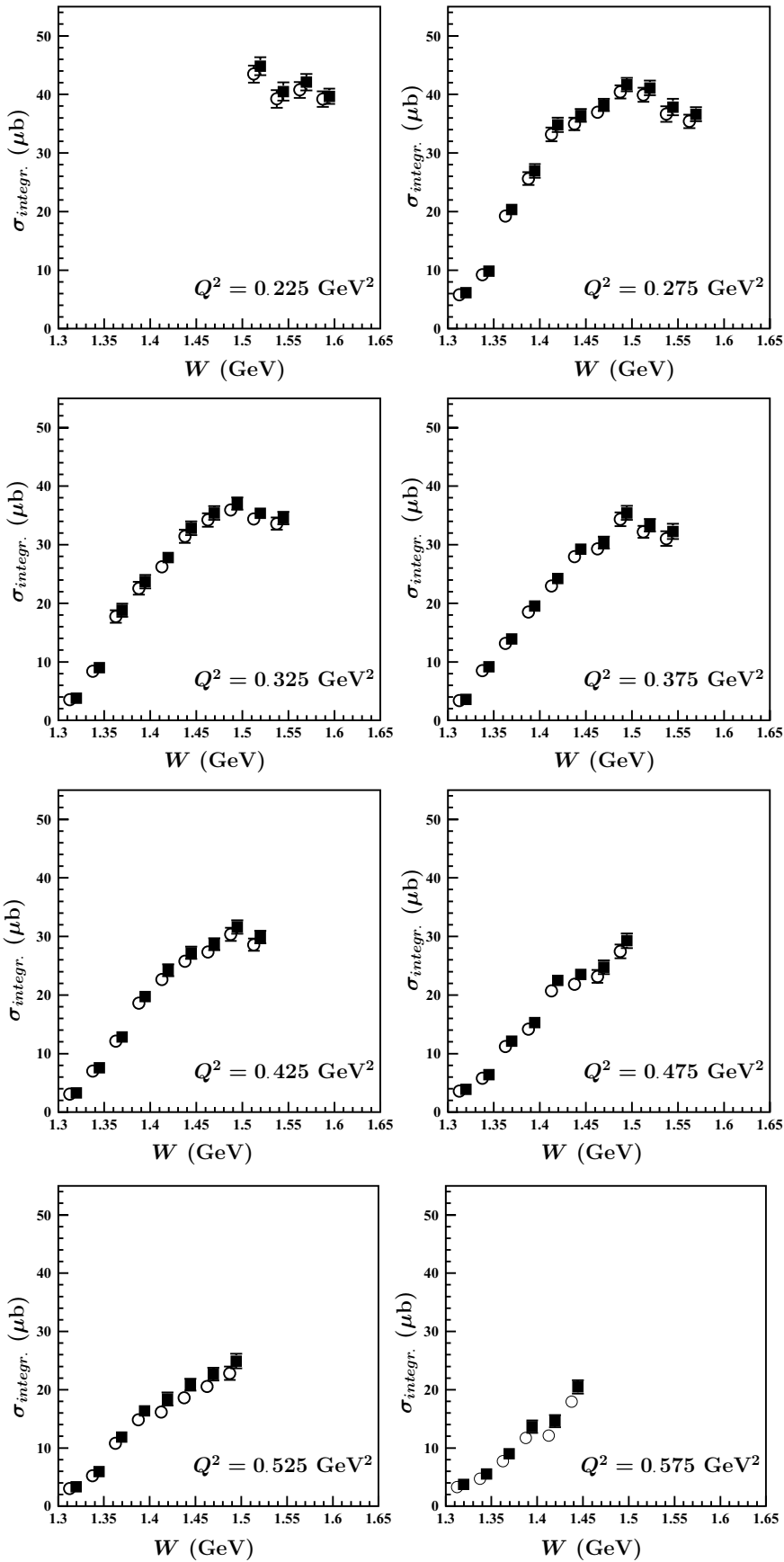


FIG. 8. Comparison of fully integrated charged double pion cross sections, obtained with (squares) and without (open circles) accounting for contributions from the CLAS areas of zero acceptance, as described in Sec. V C.

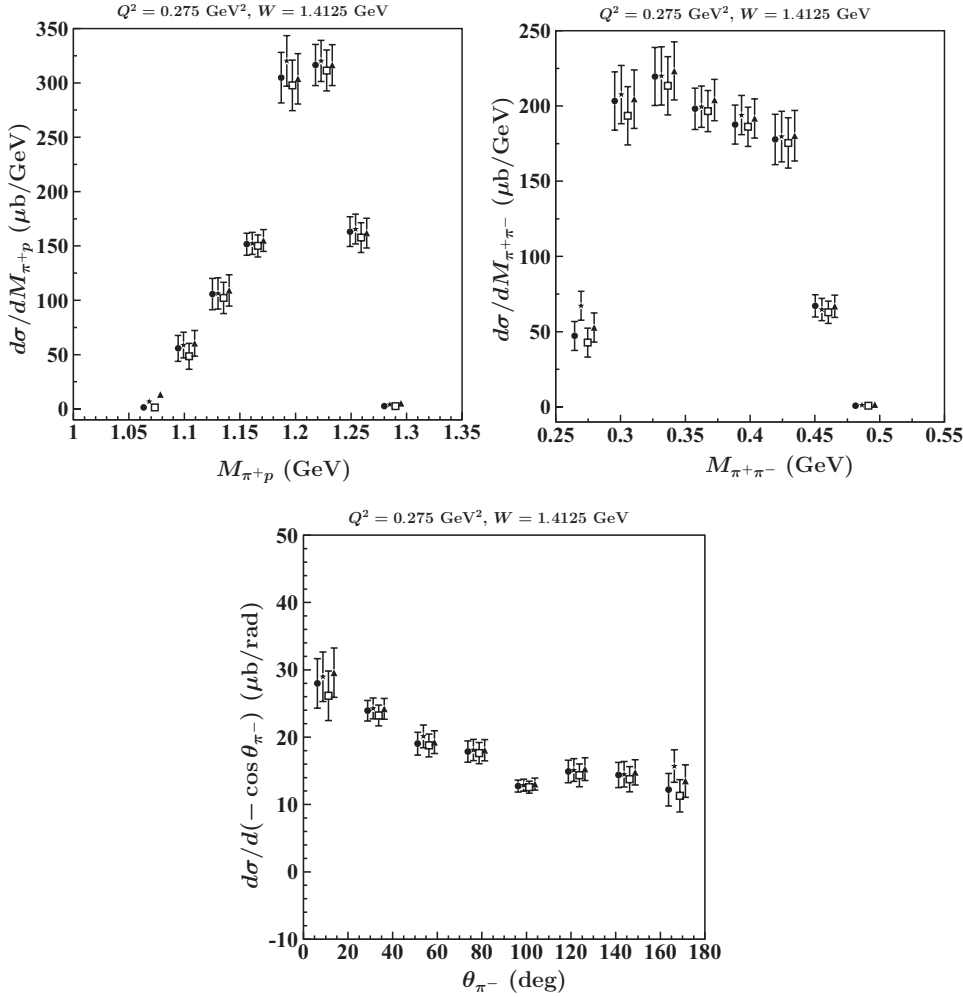


FIG. 9. Mass distributions of  $p\pi^+$  (top left) and  $\pi^+\pi^-$  (top right), and  $\pi^-$  angular (bottom) distributions, obtained from different ways of interpolating the five-fold differential cross sections into the CLAS areas of zero acceptance. Open squares correspond to one-fold differential cross sections estimated without the contributions from the CLAS areas of zero acceptance. One-fold differential cross sections, obtained with the  $R_j$  coefficients in Eq. (10) calculated within the framework of the JM03 and JM05 models, are shown by triangles and stars, respectively. One-fold differential cross sections, estimated by excluding contributions from  $\phi$ -dependent parts in Eq. (9) are shown by full circles. Note that points are spread out for clarity.

The  $\phi_i$  angular distributions were obtained as integrals from the five-fold differential cross sections over the other four variables. The  $B'$  and  $C'$  terms should be equal to zero, since these terms are integrated over the  $\alpha_i$  angles. The contributions from  $B$  and  $C$  in Eq. (9) range from 10% to 50%. For the majority of bins in  $Q^2$  and  $W$ , these contributions range from 15% to 25%. The upper limit for the model dependence of the  $A$  coefficients has been estimated by replacing in Eq. (10) all cosines by unity and by assuming  $\Delta\tilde{\varphi}/2\pi \sim 0.2$  for the geometrical coverage of the zero acceptance areas. With these assumptions, we can calculate the model uncertainty of the  $A$  coefficients as the product of the maximal contribution from the  $\varphi$ -dependent parts to the five-fold differential cross section  $(0.5)^2$  and the geometrical coverage of the CLAS areas of zero acceptance (0.2), resulting in an upper limit of 10%. However, this limit was obtained with extremely conservative estimates for the integrands in Eq. (10), the CLAS areas of zero acceptance  $\Delta\tilde{\varphi}/2\pi$ , and the relative contributions of the  $\phi$ -dependent parts. More realistic estimates, outlined below, result in uncertainties of a few percent.

In Fig. 9, we compare the results obtained using various models to estimate  $R_j$ . The JM03 and JM05 models are

rather different in the description of the five-fold differential cross sections. The JM05 approach provided a much improved treatment for the direct charged double pion electroproduction mechanisms [32]. It also contains an additional contact term that was introduced to improve the description of the  $\pi\Delta$  isobar channels. The interpolations of the five-fold differential cross sections into the inefficient areas using these two models for  $R_j$ , and in addition taking off the contributions proportional to  $\sin 2\varphi$  and  $\sin \varphi$ , result in minor modifications well inside the statistical uncertainties.

Finally we eliminate the contributions from the  $\varphi$ -dependent parts in Eq. (10) and estimate the  $A$  coefficients from data in the populated bins. The results are shown in Fig. 9 (diamonds). Again, the estimated cross sections are well inside the statistical uncertainties of the data.

#### D. Event reconstruction efficiencies

A Monte Carlo event generator [61] was used to evaluate the event reconstruction efficiencies. The event generator contains the main meson production channels in the resonance region. The efficiency for detection of the  $p\pi^+\pi^-$  in the final state was studied in detailed simulations that included the  $2\pi$  as well as  $3\pi$  final states. The latter were needed

<sup>2</sup>Ratio sum of  $\varphi$ -dependent parts over the full cross section.

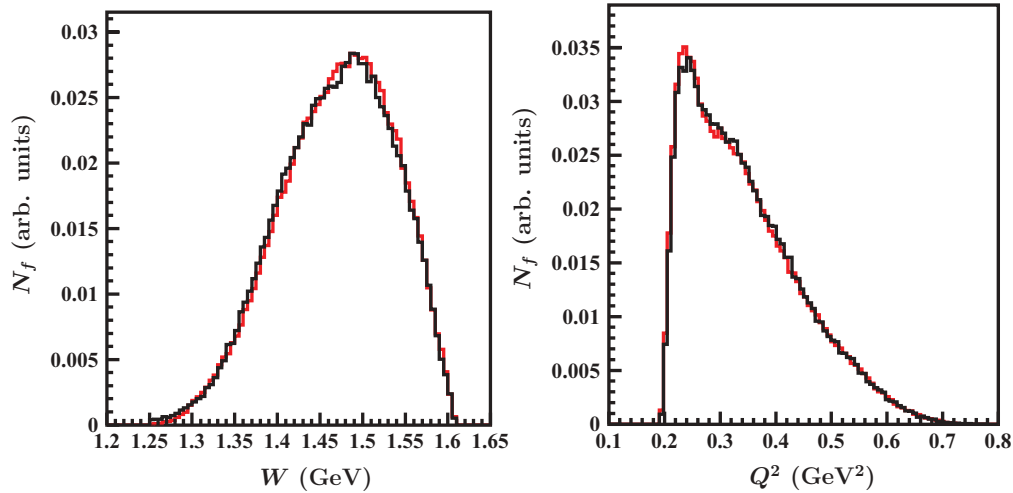


FIG. 10. (Color online)  $W$  and  $Q^2$  distributions for measured and accepted MC events ( $N_f$ ), normalized to unity. The black lines represents data; the gray (red) lines, simulation.

to account for multi-pion background in the selection of charged double pion events, when applying exclusivity cuts. These events were processed using the same reconstruction program,<sup>3</sup> event selection procedures, and fiducial cuts as for the events collected in the experiment. Efficiencies in the seven-fold differential bins were determined as the number of reconstructed events over the number of generated events and used in Eq. (1) to evaluate the five-fold differential cross sections.

As can be seen from Figs. 10 and 11, the  $W$  and  $Q^2$  dependencies are well reproduced, as are major features in the event distributions over the final state hadronic variables. Differences between the measured and simulated distributions seen for the  $\pi^+p$  invariant mass and  $\pi^-$  angular distributions

have little impact, as efficiencies inside these areas are smooth. The event generator is therefore adequate for evaluating the event reconstruction efficiency for major parts of the kinematic range covered in the experiment.

The limited phase space available for events in the low mass region with  $W < 1.40$  GeV requires a different approach to determining the event reconstruction efficiencies for the invariant mass distributions. In this region, we found rapid variations of efficiency from invariant masses inside the bins at the lowest edges for all mass distributions. The use of an event generator that closely reflects the measured distributions is crucial in this area, where no  $2\pi$  electroproduction data were previously available. Therefore, we have used an iterative procedure starting with the model event generator described above, and extracted approximate cross sections for the different mass distributions. These were then used as a realistic input into the generated event distributions over invariant masses  $W_{\text{gen}}(M_k)$  ( $k = \pi^+p, \pi^-\pi^+, \pi^-p$ ) for an accurate determination of event reconstruction efficiencies and cross sections.

<sup>3</sup>The correction factor that accounted for the events eliminated by the cut on the number of photoelectrons in the Cherenkov counter was applied for the measured events only.

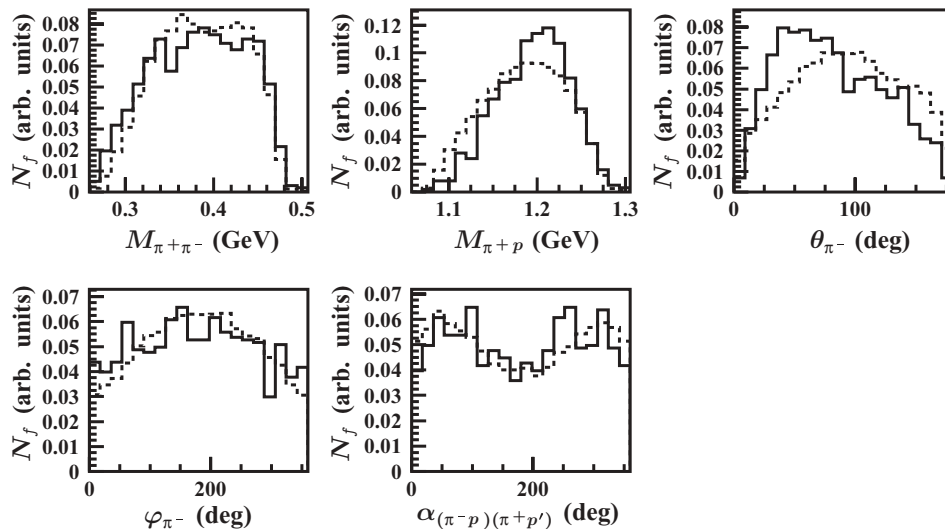


FIG. 11. Comparison between measured (solid lines) and simulated (dashed lines) event distributions normalized to unity ( $N_f$ ) for various final state variables. ( $W = 1.4125$  GeV,  $Q^2 = 0.525$  GeV<sup>2</sup>).

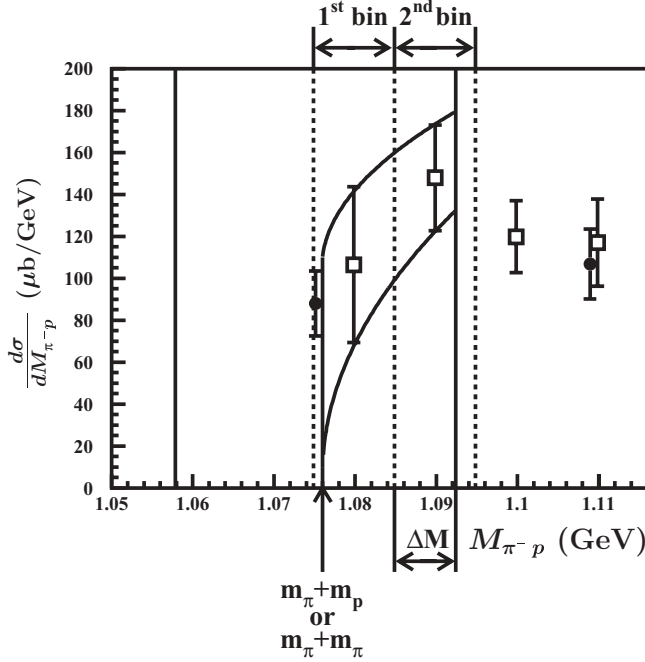


FIG. 12. Corrections for mass distribution in the cross sections near threshold. The filled circles represent the preliminary cross sections obtained with the nominal bin size. The lowest mass bin of nominal size is shown by the solid vertical lines. Preliminary cross sections obtained using a bin size reduced by a factor of 4 are shown by the open squares. The mass bins of reduced size are shown by the vertical dashed lines. The bin of lowest invariant masses  $\Delta M$ , where corrected cross sections were evaluated, covers the interval from the dashed to the solid lines connected by the double-sided arrow. Corrected cross sections are given by the integrals from interpolating curves inside the  $\Delta M$  bin over the bin width.

The improved estimates of event reconstruction efficiencies for the mass distributions  $\epsilon_{\text{imp}}(M_k)$  were obtained as

$$\epsilon_{\text{imp}}(M_k) = \frac{W_{\text{meas}}(M_k)\epsilon(W, Q^2)}{W_{\text{gen}}(M_k)}, \quad (11)$$

where  $W_{\text{meas}}(M_k)$  are event distributions in the invariant mass  $M_k$  and taken from the data. Both measured  $W_{\text{meas}}(M_k)$  and generated  $W_{\text{gen}}(M_k)$  ( $k = \pi^+p$ ) event distributions were normalized to unity. The quantity  $\epsilon(W, Q^2)$  is the event reconstruction efficiency in a particular  $(W, Q^2)$  bin and was estimated using the event generator.

A comparison of the mass distribution obtained using the event generator with those estimated from Eq. (11) after further corrections, described in the Sec. VE, is shown in Fig. 13.

### E. Corrections for mass distributions

After all the previously discussed acceptance corrections were made, several mass distributions needed further correction to account for the rapid variation of the cross sections inside some of the mass bins. For these bins, the cross sections were reevaluated, using a binning size reduced by a factor of 4. Cross sections at the nominal grid were compared to those obtained at the grid of reduced bin size and interpolated into

the nominal grid. In case of discrepancies, interpolated values of the cross sections were used, since they were determined with better mass resolution.

A special procedure was developed to evaluate the cross sections at the smallest invariant masses using constraints on the amplitude behavior near the phase-space limits. All mass distributions at the smallest invariant masses were reevaluated using a binning size reduced by a factor of 4 and interpolated over invariant masses in a way compatible with general requirements on a power law amplitude behavior near threshold:

$$\frac{d\sigma}{dM_k} \left[ \frac{\mu\text{b}}{\text{GeV}} \right] = \begin{cases} C(M_{\pi^-p(\pi^+p)} - 1.076)^\alpha, & M_{\pi^-p(\pi^+p)} > 1.076 \text{ GeV}, \\ 0, & M_{\pi^-p(\pi^+p)} < 1.076 \text{ GeV}, \\ C(M_{\pi^+\pi^-} - 0.276)^\alpha, & M_{\pi^+\pi^-} > 0.276 \text{ GeV}, \\ 0, & M_{\pi^+\pi^-} < 0.276 \text{ GeV}, \end{cases} \quad (12)$$

where  $C$  and  $\alpha$  are free parameters fit to the cross sections obtained with better mass resolution. The corrected cross sections were not evaluated in the mass areas closest to the threshold, which were affected considerably by the event migration. The bins of smallest invariant masses cover the mass intervals from the left edge of the next-to-smallest mass bin of regular size to the right edge of the smallest mass bin of reduced size (Fig. 12). Differential cross sections in these bins were computed as integrals from interpolating curves inside the bins divided by the bin size  $\Delta M$ . The two solid curves in Fig. 12 represent interpolating curves fit to the upper and lower boundaries of preliminary cross sections obtained with these improved mass binnings. Differences in the corrected cross sections, calculated using these two interpolations, give us the systematic uncertainties. These corrections only affect the lowest mass bins near the phase-space limit. At larger invariant masses, the cross sections were determined with the nominal bin size as described in the Sec. VB.

The comparison of mass distributions before and after all corrections described in Secs. VD and VE is shown in Fig. 13.

### F. Radiative corrections

Radiative processes were evaluated using the procedure of Mo and Tsai [66] developed for inclusive processes and incorporated in the event generator [61]. Approaches that are capable of describing radiative processes in exclusive  $2\pi$  electroproduction are not yet available.

The radiative correction factor  $R$  was determined as

$$R = \frac{N_{\text{rad}}}{N_{\text{norad}}}, \quad (13)$$

where  $N_{\text{rad}}$  and  $N_{\text{norad}}$  are the numbers of generated events in each  $(W, Q^2)$  bin with radiative effects switched on and off, respectively. This factor  $R$  was used in Eq. (1) for calculations of the five-fold differential cross sections.

The particular hadronic tensor for exclusive  $2\pi$  electroproduction has impact mostly on radiation of the hard photons

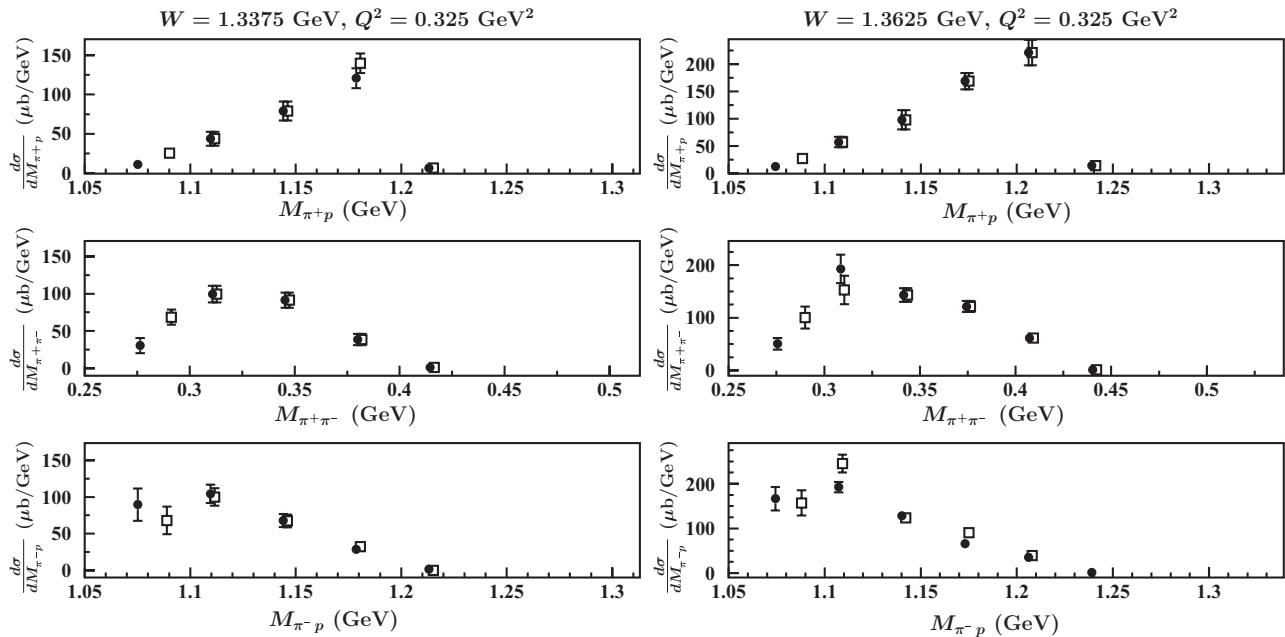


FIG. 13. Comparison of mass distribution cross sections before (filled circles) and after (open squares) improvements, described in Secs. VD and VE.

by the ingoing and scattered electrons. Moreover, its influence on observables decreases after integration over the final state kinematic variables [67]. The inclusive procedure for radiative corrections represents a reasonable approximation for the case of our data, since we applied an exclusivity cut, which restricts the hardness for the emitted photons, and all one-fold differential cross sections represent integrals of the five-fold differential cross sections over four kinematic variables.

We found that the relative contributions of hard photons to  $R$  varied by 30–50%. It is only this contribution that could be affected by the hadronic tensor and may be different in various exclusive channels.

In Ref. [67] the effect of integration over kinematic variables for the case of the exclusive single pion electroproduction was studied, for which radiative processes have been evaluated exactly with the hadronic tensor derived from the fit to data. It was found that radiative corrections are reduced by factors of 2 to 4 after integration over the  $\varphi$  angle for the emitted pion. Therefore, integration over four variables in the case of charged double pion electroproduction is expected to reduce the radiative correction factor considerably, at least by a factor of 4 [67].

Radiative corrections in the kinematics of this measurement were found to be less than 20%. Therefore the contribution due to hard photon emission to the radiative corrections should be less than 10%. They should be further reduced by more than a factor of 4 after integration of the five-fold differential cross sections over four variables. Even a large uncertainty of 100% in the contributions of hard photons would result in uncertainties of the overall radiative corrections to charged double pion cross section of only a few percent.

The uncertainty in determining the cross sections caused by using the inclusive approximation for radiative corrections

is well below the statistical uncertainties of the data and is included in the systematic uncertainties.<sup>4</sup>

### G. Results and systematic uncertainties

In our analysis, we determined nine one-fold differential cross sections in each  $(W, Q^2)$  bin at invariant masses of the hadronic system from 1.30 to 1.57 GeV and at photon virtualities from 0.2 to 0.6 GeV<sup>2</sup> with bins in  $W$  of 25 MeV and in  $Q^2$  of 0.05 GeV<sup>2</sup>. The data consist of  $\pi^+p$ ,  $\pi^-\pi^+$ , and  $\pi^-p$  invariant mass distributions, as well as  $\pi^-$ ,  $\pi^+$ , and proton angular distributions, and three distributions over angles  $\alpha_i$  ( $i = 1, 2, 3$ ) defined in Sec. VA. The full data set, consisting of 4695 cross sections, may be found in Ref. [22]. Fully integrated cross sections are shown in Figs. 15 and 16. These results represent the first comprehensive data set for charged double pion electroproduction at  $Q^2 < 0.6$  GeV<sup>2</sup>. With respect to the previous data [20], the bin size in  $W$  is reduced by almost a factor of 10, while the binning in  $Q^2$  is reduced by a factor of 5.

Systematic uncertainties averaged over the kinematic range covered by the data are presented in Table I. In the following, we discuss the various contributions to the systematic uncertainties in more detail.

To estimate uncertainties in the integration procedure, we compared the values of the fully integrated cross sections obtained by integration over three sets of kinematic variables,

<sup>4</sup>The information obtained on the hadronic tensor from our JM model [33] based on a fit to the charged double pion data represents valuable input for the future development of a fully exclusive radiative correction procedure for double pion electroproduction.

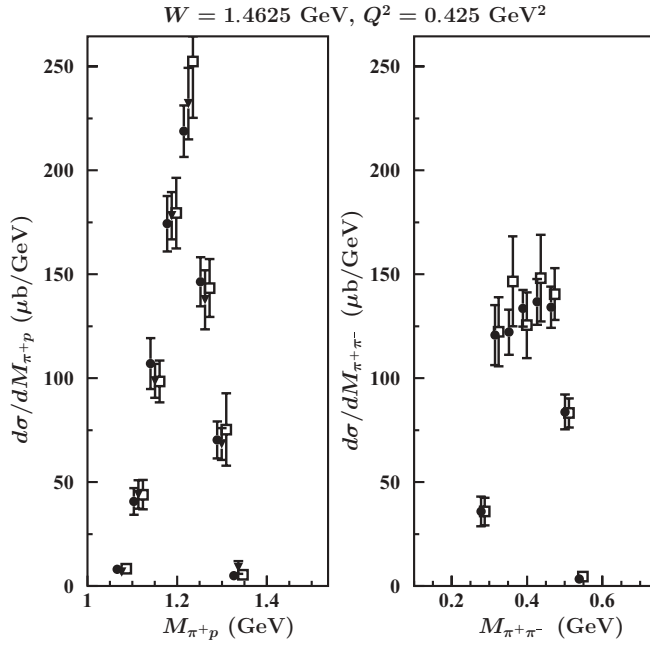


FIG. 14. Comparison between  $\pi^+p$  and  $\pi^-\pi^+$  mass distribution cross sections, obtained by integration of the five-fold differential cross sections for various choices of the final state kinematic variables (choices from 1 to 3 are shown by full circles, open squares, and triangles, respectively), defined in the Sec. VA.

defined in Sec. VA. The ratios of r.m.s values for the integrated cross sections over their mean values were treated as systematic uncertainties related to the integration procedure. They are maximal at the lowest  $W$  value for all photon virtualities, and range from 5% to 7%. As  $W$  increases, they drop to  $\sim 1\%$  at the highest  $W$  value.

To estimate the uncertainties in the integration procedure for the one-fold differential cross section, we compared their values determined in integration of the five-fold differential cross sections, obtained with three different choices of the final state variables, described in Sec. VA. When calculating these integrals for various kinematic variables, different sets of five-dimensional bins contribute to the respective integrals. The efficiency was estimated for each set independently. Moreover, different inefficient areas contribute to the same cross sections estimated from integration over various kinematic grids. Therefore, a comparison of fully integrated and one-fold differential cross sections, obtained by integration over various kinematic variables, allows us to check the accuracy of the detector efficiency evaluations and propagation of the five-fold differential cross sections in the CLAS areas of zero acceptance.

Each of the three kinematic grids, discussed in Sec. VA, contains the  $\pi^+p$  invariant mass distribution, while just two grids contain  $\pi^-\pi^+$  invariant masses. The angles describing the final state particles have unique assignments for each of three kinematic grids. We can therefore compare the results of integrations over three different kinematic grids for the  $\pi^+p$  mass distributions. For the  $\pi^-\pi^+$  mass distributions, the integration over two grids can be compared. We found that these one-fold differential cross sections coincide well

within their statistical uncertainties and in the entire range of kinematics covered by measurements. As an example, in Fig. 14 we show the comparison of mass distributions at  $W = 1.41$  GeV and  $Q^2 = 0.425$  GeV<sup>2</sup>, with the ones obtained from integrating the five-fold differential cross sections over different sets of kinematic variables. The comparison of the fully integrated cross sections is shown in Fig. 15. The results differ by only a fraction of the statistical uncertainties.

The main contributions to the uncertainty in the overall cross section normalization are given by uncertainties in the integrated luminosity and the electron detection and reconstruction efficiencies. These contributions have been estimated by measuring the well-known elastic  $ep$  scattering cross sections. The comparison with a parametrization [63] of the world data shows that the overall normalization is within a  $\sim 5\%$  uncertainty.

To evaluate the systematics involved in defining the final state exclusive process, we varied the missing mass cut used to identify the unmeasured  $\pi^-$  and modified the fiducial regions where final state particles are selected. The average uncertainties are shown in Table I.

In Sec. VC we concluded that the contributions of the zero acceptance regions in CLAS affect the extracted differential and integrated cross sections well within the statistical uncertainties. Systematics uncertainties related to propagating the data into the inactive areas of CLAS were estimated, assuming a 50% uncertainty in the extrapolation of the five-fold differential cross sections, resulting in 2–5% uncertainties, and increasing in  $Q^2$ .

The global systematics for radiative corrections, listed in the Table I, were calculated assuming the individual contributions are uncorrelated. The factor  $R$ , obtained from our Monte Carlo simulation (Sec. VF), revealed no  $Q^2$  dependence in the entire kinematic range of our measurements. The r.m.s. values for the  $R$  factors calculated at various  $Q^2$  were assigned to the uncertainties for the radiative correction factor. Based on the estimates described in Sec. VF, we assigned an upper limit of 2.5% to the uncertainties related to the hard photon emission.

The overall systematic uncertainty shown in Table I was obtained as the square root of the quadratic sum over the individual contributions. Applying the described procedures in each bin of  $W$  and  $Q^2$  individually, we obtain the systematic

TABLE I. Summary of systematic uncertainties for the fully integrated cross sections. The values represent averages over the kinematic areas covered by the data.

Source	Systematic uncertainty
Integration	3%
Fiducial cuts	3%
Missing mass cut	2.5%
Normalization	<5%
Binning effects	3%
Radiative correction	<3.5%
Acceptances	3%
Total	<9%

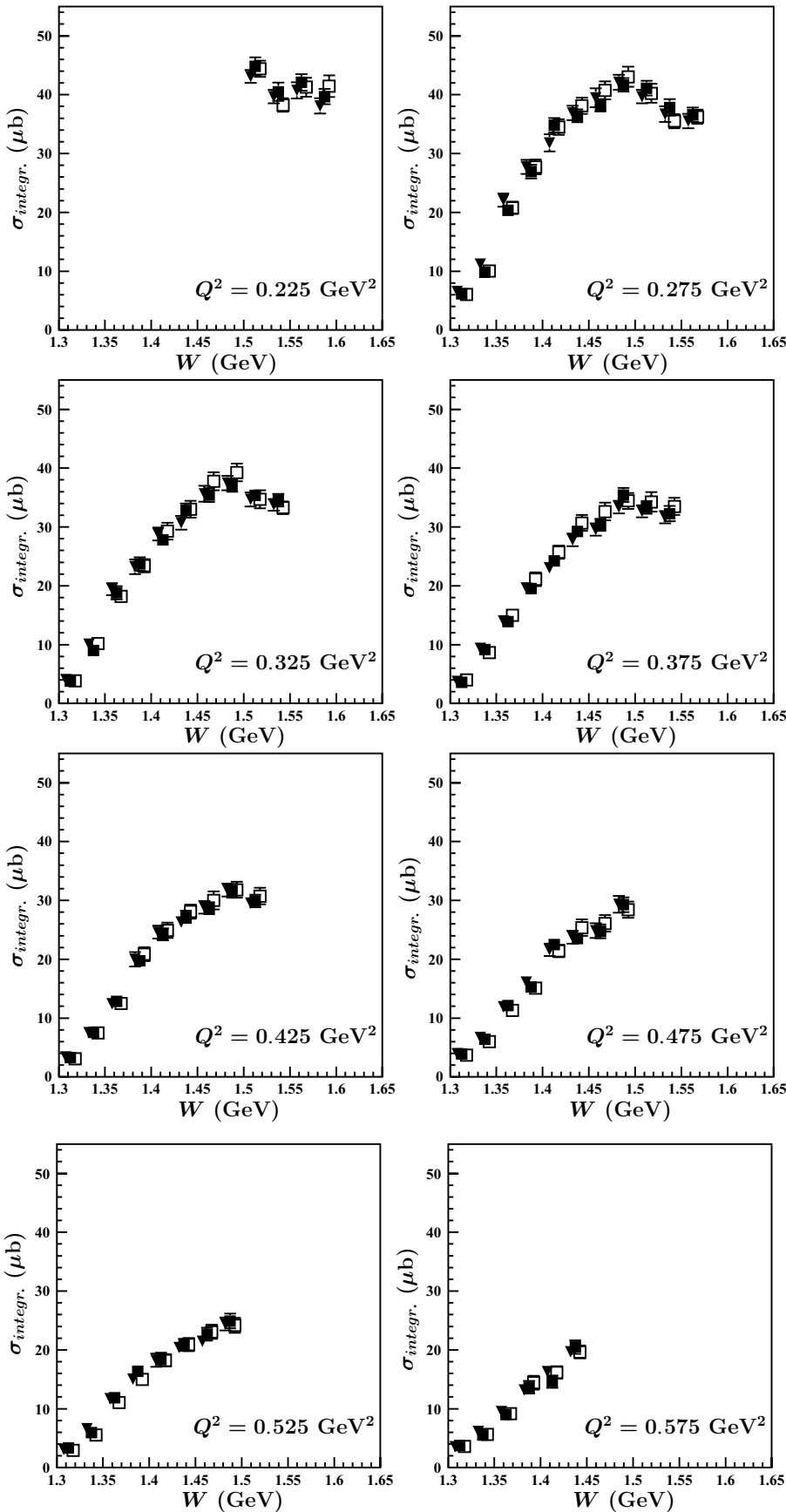


FIG. 15. Comparison between fully integrated charged double pion cross sections, obtained in the integration of the five-fold differential cross sections over three various choices of the final state variables, described in the Sec. V A. Choices 1–3 for kinematic variables are shown by triangles and the open and full squares, respectively.



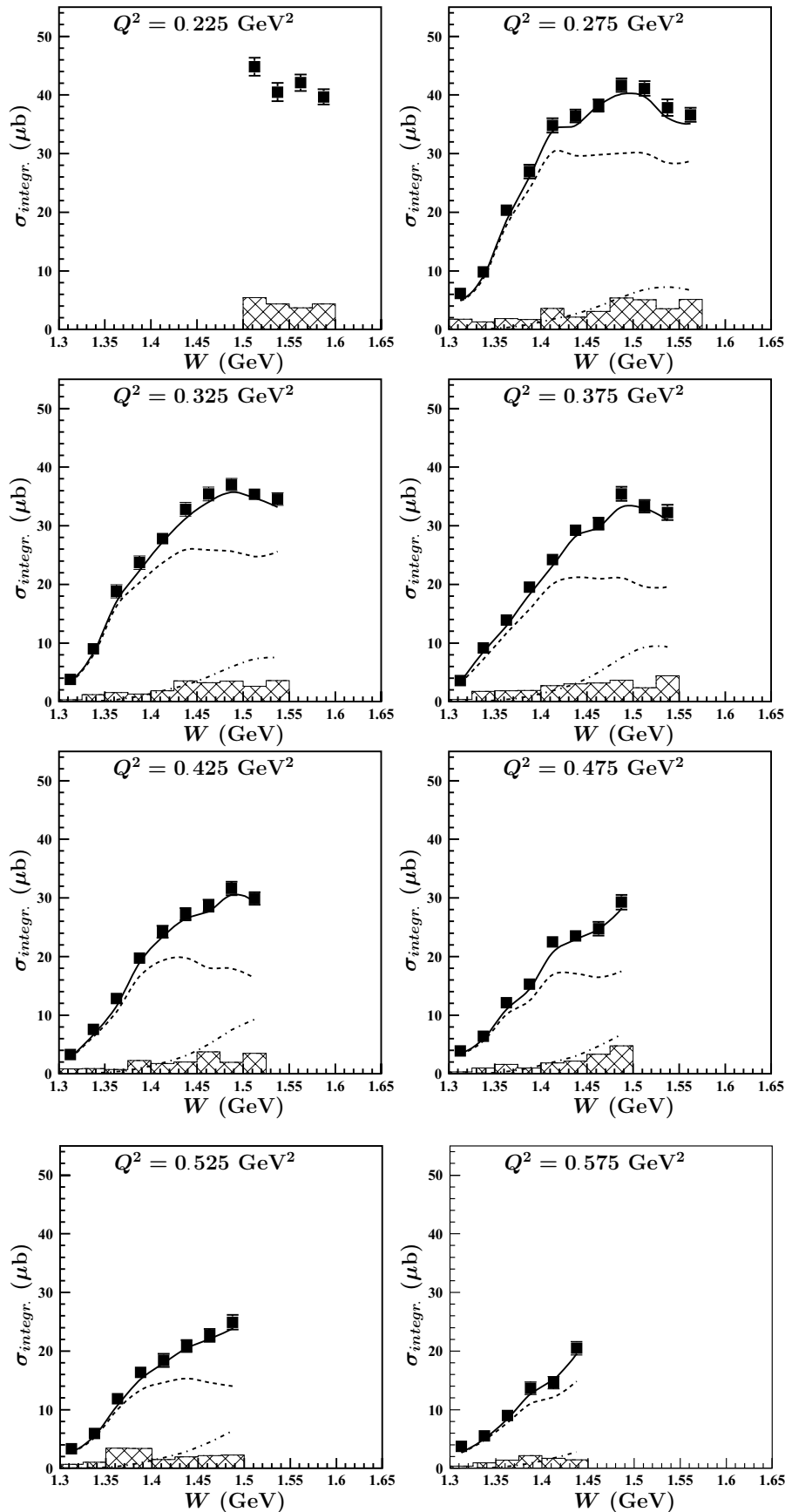


FIG. 16. Fully integrated  $2\pi$  cross section at various  $Q^2$ . Crossed areas represent systematic uncertainties. Full calculations within the framework of the JM06 model [33] are shown by solid curves. The contributions from  $s$ -channel resonances and from nonresonant mechanisms are shown by the dot-dashed and dashed curves, respectively.

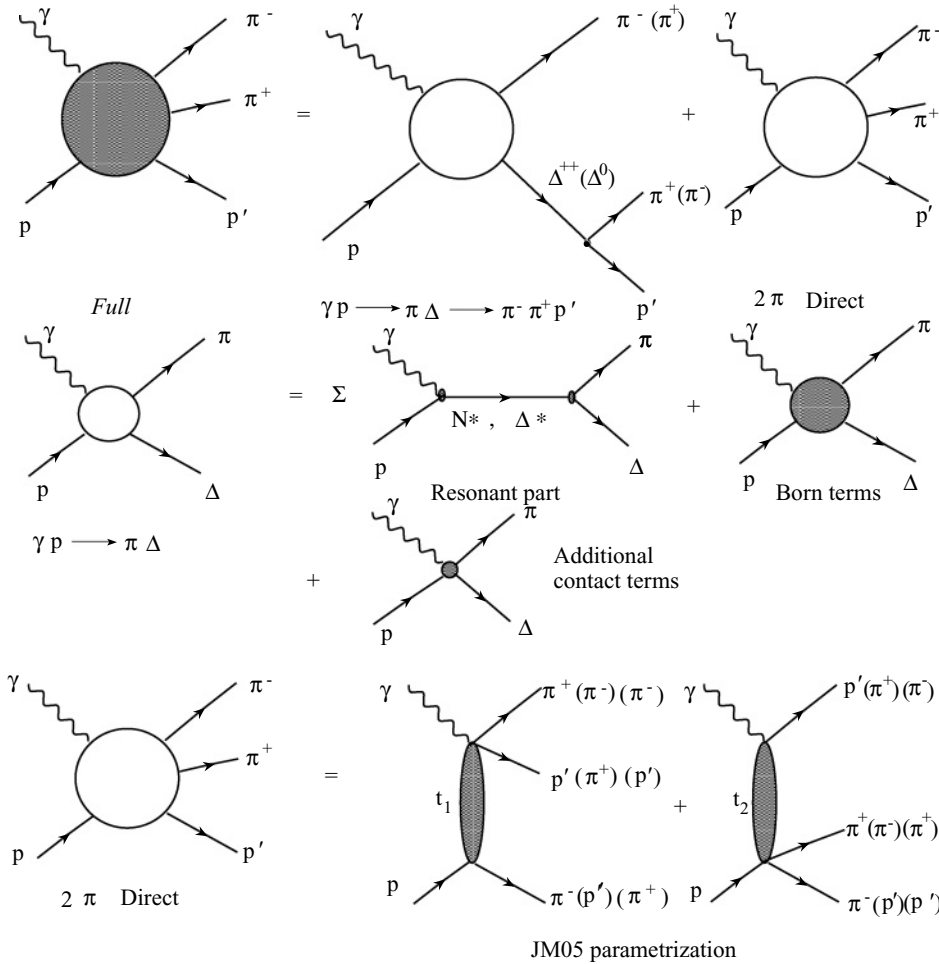


FIG. 17. The mechanisms of JM05 model [32,52] contributing to  $2\pi$  electroproduction at low  $W$  and  $Q^2$ .

uncertainties for the integrated cross sections as shown by the crossed areas in Fig. 16.

## VI. PHENOMENOLOGICAL ANALYSIS

The comprehensive information on the one-fold differential cross sections for charged double pion production provided by the data enabled us to carry out a combined analysis of the nine one-fold differential cross sections in each  $W$  and  $Q^2$  bin, and to establish all significant mechanisms contributing to charged double pion electroproduction in the range  $W < 1.6$  GeV and  $Q^2 = 0.2\text{--}0.6$  GeV<sup>2</sup>. Before our data were available, the information on  $2\pi$  electroproduction mechanisms in this kinematic area was rather scarce and quite uncertain.

The presence and strengths of the contributing  $2\pi$  electroproduction mechanisms were established by studying the kinematic dependencies in differential cross sections and their correlations in a variety of available observables. The analysis was carried out using a phenomenological model developed in the past few years by the Jefferson Laboratory–Moscow State University (JM) Collaboration [32,33,48,54,55]. Within the JM model developed up to 2005, called JM05, we succeeded in describing previous CLAS charged double pion electroproduction data [21] that consisted of three invariant

masses and  $\pi^-$  angular distributions at  $W$  from 1.4 to 2.1 GeV and at the photon virtualities from 0.5 to 1.5 GeV<sup>2</sup>.

Analysis of the recent CLAS  $2\pi$  data, presented in this paper, allowed us to study the still unexplored kinematics area of photon virtualities from 0.25 to 0.6 GeV<sup>2</sup>. Our knowledge of the contributing mechanisms was extended considerably, resulting in the recent version of the JM model, which we refer to as JM06. A detailed description of the JM06 model version may be found in a separate paper [55]. Here we discuss the basic ingredients of JM05/JM06 model versions and the major results.

The  $\gamma^* p \rightarrow \pi^+ \pi^- p$  production amplitude within these model versions are illustrated in Figs. 17 and 19. They consist of the  $\pi^- \Delta^{++}$ ,  $\pi^+ \Delta^0$  isobar channels and direct double pion production mechanisms. The production amplitudes for  $\pi \Delta$  intermediate states consist of the resonant contributions  $\gamma N \rightarrow N^*, \Delta^* \rightarrow \pi \Delta$ , shown in the second row of the Fig. 17 and nonresonant terms. In the kinematic area covered in our measurements, only the  $P_{11}(1440)$  and  $D_{13}(1520)$  nucleon resonances have the contributions in one-fold differential cross sections, which are outside of the data uncertainties. The nonresonant amplitudes, shown in right diagram in the second row of Fig. 17, were calculated from the well-established Born terms and presented in Ref. [49,55]. Additional contact terms were implemented to

account for possible contributions from other mechanisms to  $\pi\Delta$  production, as well as for hadronic interactions of  $\pi\Delta$  states with other open channels [32,54]. A parametrization for these amplitudes may be found in Ref. [55].

The contributions from all isobar channels combined account for 70–90% of the charged double pion fully integrated cross sections in the kinematic area covered in our measurements. A remaining part of cross sections comes from direct charged double pion ( $2\pi$ ) production mechanisms, when the  $\pi^+\pi^-p$  final state is created without the formation of unstable hadrons in the intermediate states. The diagrams in the bottom of Fig. 17 represents the direct  $2\pi$  production mechanisms in the JM05 model version. They were parametrized in terms of a contact vertex and an unspecified particle-exchange amplitude, described by the effective propagator, that depends exponentially on a running four-momentum squared [33,52]. This parametrization allowed us to reproduce steep dependencies in  $\pi^-$  angular distributions at the backward angles, clearly seen both in the previous CLAS charged double pion electroproduction data [21] at  $Q^2$  and in the data of this paper. The example is shown in Fig. 18.

The JM05 model describes successfully the recent CLAS data on three invariant masses and  $\pi^-$  angular distributions in the entire kinematic area covered by measurements, confirming the important role of direct  $2\pi$  production mechanisms at the photon virtualities from 0.25 to 0.60  $\text{GeV}^2$ . However, the JM05 model was unable to reproduce the data on  $\pi^+$  and  $p$  angular distributions. This failure has become evident at  $W > 1.40$   $\text{GeV}$  and for all photon virtualities mentioned above. We see in Fig. 18 considerable differences between the data and the predicted  $\pi^+$  and  $p$  angular distributions due to direct  $2\pi$  production mechanisms (dashed curves). It is therefore necessary to improve the description of direct  $2\pi$  production amplitudes.

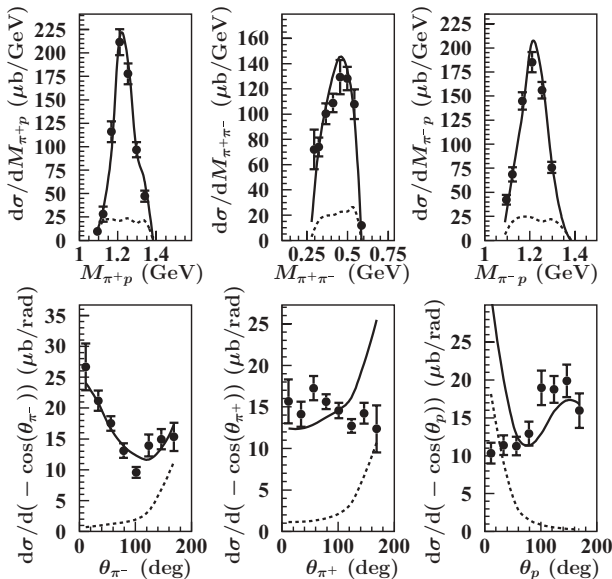


FIG. 18. CLAS  $p\pi^+\pi^-$  data compared with JM05 calculations (solid lines). The contributions from direct  $2\pi$  production, resulting in discrepancies in the description of  $\pi^+$  and  $p$  angular distributions, are shown as dashed lines.

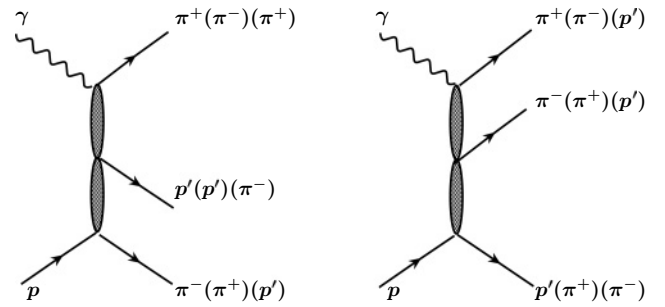


FIG. 19. Direct charged double pion production mechanisms in JM06 model.

In the JM06 model employed in this work, the contact interactions in direct  $2\pi$  production processes were replaced by additional exchange mechanisms, as shown in Fig. 19. The propagators in both unspecified exchange mechanisms were parametrized by the same exponential dependence on a running four-momentum squared with the slope parameter  $b$  fit to the data and equal to  $4.0 \text{ GeV}^{-2}$ . The parametrization of direct  $2\pi$  production amplitudes in the JM06 model may be found in Ref. [55].

Within the framework of the JM06 approach, we were able to describe the  $2\pi$  data of our paper in the entire kinematic range covered by the measurements. As a typical example, the model description of the nine one-fold differential charged double pion cross sections at  $W = 1.51$   $\text{GeV}$  and  $Q^2 = 0.425$   $\text{GeV}^2$  is shown in Fig. 20 together with the contributions of all mechanisms incorporated in the JM06 description. Our analysis revealed a dominant contribution from the  $\pi^-\Delta^{++}$  isobar channel. A major role of this channel at the  $W$  area covered by our measurements ( $W < 1.6$   $\text{GeV}$ ) was also established in analysis of the data on charged double pion photoproduction [68,69]. In this kinematic area, nucleon resonances contribute to  $\pi\Delta$  channels only. Dominant  $\pi\Delta$  contributions established in our data analysis suggest sensitivity of measured one-fold differential cross sections to the resonance excitation. The information on the contributions of  $\pi\Delta$  channels to charged double pion electroproduction will be useful for the development of microscopic models which describe the isobar channels by explicit meson-baryon diagrams [25–27,41,42,70]. Moreover, the data on contact amplitudes, incorporated into the sets of  $\pi\Delta$  Born terms, open up an opportunity for future studies of the  $N \rightarrow \Delta$  axial transition form factor.

The shapes of the cross sections shown in Fig. 20 for the different mechanisms are substantially different in the various observables but highly correlated by the reaction dynamics. Moreover, we found no need to implement additional mechanisms beyond the ones already included in JM06. Therefore, the successful description of all nine one-fold differential charged double pion cross sections allowed us to identify all essential contributing processes and access their dynamics at the phenomenological level. To check the robustness of the results obtained within the framework of the JM06 model, we fitted the model parameters to a limited set of data that included only six differential cross sections: all three invariant masses and three angular  $\theta_i$  ( $i = \pi^-, \pi^+, p$ ) distributions for

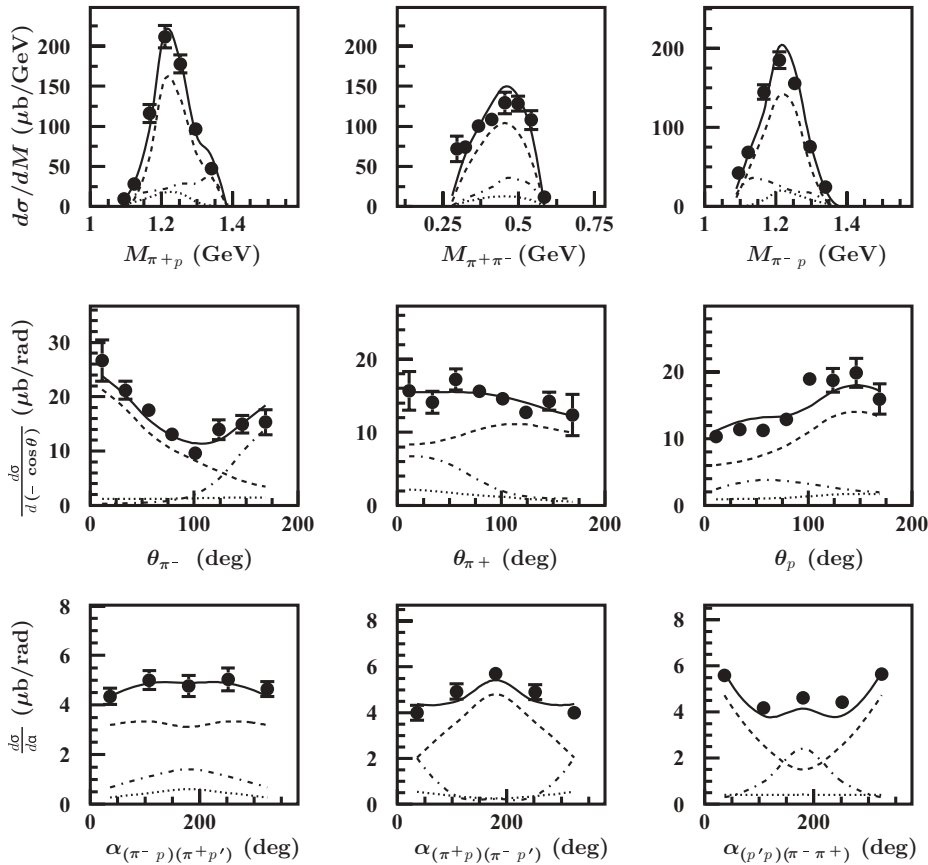


FIG. 20. CLAS charged double pion differential cross sections at  $W = 1.51$  GeV and  $Q^2 = 0.425$  GeV<sup>2</sup> within the framework of the JM06 model. The full calculations are shown by the solid lines. The contributions from  $\pi^- \Delta^{++}$  and  $\pi^+ \Delta^0$  isobar channels are shown by the dashed and dotted lines, respectively. The contributions from direct charged double pion production processes are shown by the dot-dashed lines.  $\alpha_i$  angular distributions were calculated with the JM06 parameters fit to the other six differential cross sections.

the final state hadrons. The remaining three distributions over the  $\alpha_i$  angles were calculated, keeping the JM06 parameters fixed. A good description of all  $\alpha_i$  distributions was achieved throughout the kinematics covered by the measurements, giving us confidence that all essential processes are described within the JM06 model.

Analysis of charged double pion electroproduction data also allowed us to obtain the information on nonresonant amplitudes in  $\pi \Delta$  isobar channels, decomposed over the set of partial waves of different total angular momentum  $J$ . These results are described in Ref. [55]. The partial waves derived from our data will be used in the combined analysis of major single and double pion electroproduction channels within the framework of advanced coupled-channel formalism, such as that developed in Refs. [24–27].

The separated resonant and nonresonant contributions to the fully integrated charged double pion cross sections are presented in Fig. 16. Nonresonant mechanisms represent a major contributor in the entire kinematic area covered by our measurements. The dominant part of the resonant amplitudes comes from the  $P_{11}(1440)$  and  $D_{13}(1520)$  states combined. There is no evidence for substantial decays of the  $S_{11}(1535)$  resonance with two pion emission, while the tail from the nucleon excitations with masses above 1.6 GeV is well inside the data uncertainties. The phase-space limitations prevent  $P_{33}(1232)$  decays to the final states with two pions. So, the resonant contributions at  $W < 1.4$  GeV become too small for their reliable evaluations. However, the resonant parts of fully

integrated cross sections increase rapidly at  $W > 1.4$  GeV, where they become larger than the data uncertainties. The relative resonant contributions increase with  $Q^2$  but remain below 30%. For the studies of resonant contributions, a combined analysis of all nine one-fold differential cross sections for the first time available from our measurements becomes particularly important. Global fit of all available differential cross sections is capable of isolating the mechanisms with relatively moderate contributions to the fully integrated cross sections. For instance, analysis of all angular distributions combined allowed us to establish the direct  $2\pi$  production mechanisms with relative contributions less than 30%, which is comparable to the relative contribution from resonances.

The resonant and nonresonant parts of the differential cross sections at  $W = 1.51$  GeV and  $Q^2 = 0.425$  GeV<sup>2</sup> are shown in Fig. 21. The resonant contributions calculated with JM06 parameters adjusted to the data clearly show the data sensitivity to the resonant amplitudes. There are kinematic areas in all one-fold differential cross sections, where the contributions from the resonant and nonresonant parts are comparable. As follows from the evaluations shown in Figs. 20 and 21, the  $\pi^- \Delta^{++}$  contributions to the  $\pi^-$  angular distributions at backward angles and to  $p$  angular distributions at forward angles mostly consist of the resonant parts. The shapes of the resonant and nonresonant contributions are quite different for most differential cross sections shown in Fig. 21, especially the angular distributions. Moreover, the correlations between kinematic dependencies of the resonant/nonresonant parts in

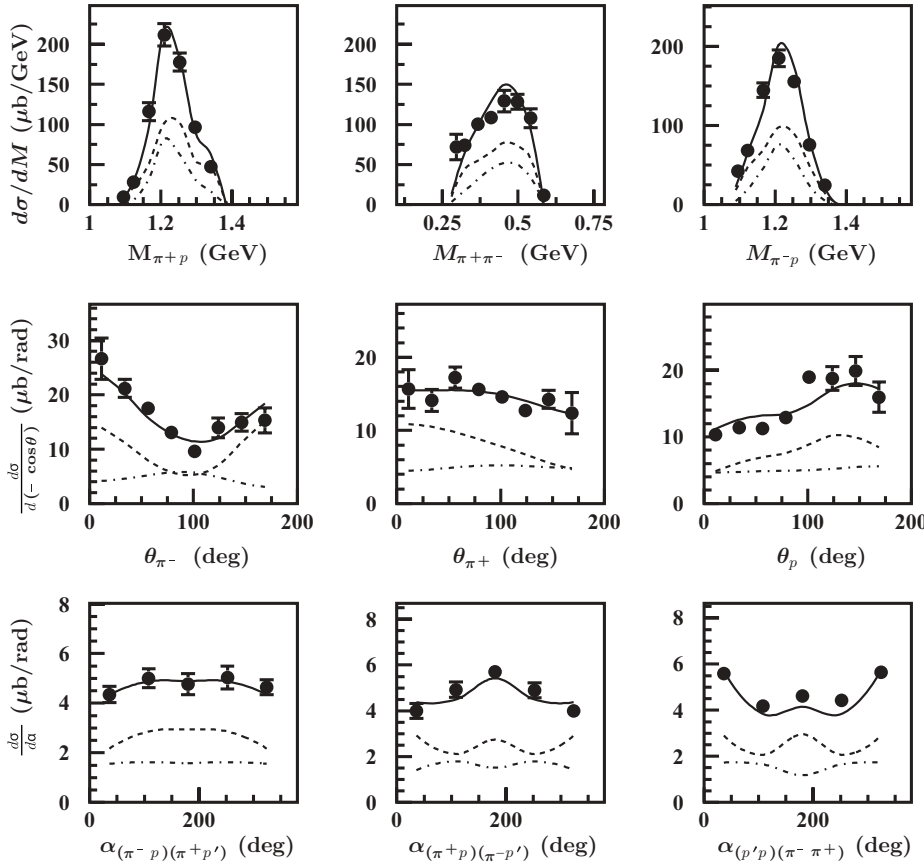


FIG. 21. Resonant (dot-dashed lines) and nonresonant (dashed lines) contributions to the charged double pion differential cross sections at  $W = 1.51$  GeV and  $Q^2 = 0.425$  GeV<sup>2</sup>. The full JM06 calculations are shown by solid lines.

various one-fold differential cross sections are also quite different. Therefore, global fits to nine one-fold differential cross sections offer an opportunity to access the resonance contributions to all measured observables.

Moreover, in the kinematic region covered by our measurements, there are also CLAS data on single pion electroproduction [4,6–9,22,71]. Only single and double pion exclusive channels contribute to the total meson production cross sections off protons at  $W < 1.5$  GeV, making this kinematic area very promising for evaluation of transition helicity amplitudes to the  $P_{11}(1440)$  and  $D_{13}(1520)$  states in full coupled-channel analysis. Advanced coupled-channel approaches are under development at Jefferson Lab [24,25,27], which will be used to determine nucleon resonance parameters from combined analysis of single and double pion electroproduction. Successful description of experimental data on all available observables in these channels with completely different nonresonant mechanisms, employing a common set of  $N^*$  electrocouplings, is vital to obtaining the transition helicity amplitudes to the  $P_{11}(1440)$  and  $D_{13}(1520)$  states at various photon virtualities.

## VII. CONCLUSIONS AND OUTLOOK

In this paper, we have presented a large body of electroproduction data for the process  $\gamma_v p \rightarrow p\pi^+\pi^-$ . The large acceptance of CLAS allowed extraction of the one-fold differential and fully integrated charged double pion cross sections.

The results were tested for robustness by using different integration grids, which showed that consistent results are obtained independent of the specific integration procedure.

One-fold differential and fully integrated cross sections were obtained for  $W$  from 1.3 to 1.6 GeV and  $Q^2$  from 0.2 to 0.6 GeV<sup>2</sup>. The high statistics and good momentum resolution of the measurements allowed us to use bin sizes of  $\Delta W = 25$  MeV and  $\Delta Q^2 = 0.05$  GeV<sup>2</sup>, which are at least a factor of 5 smaller than the ones used in previous measurements. For the first time, nine independent differential cross sections in each bin of  $W$  and  $Q^2$  were measured.

The phenomenological analysis of the cross sections within the framework of the JM06 approach [33,54,55] allowed us to establish all essential mechanisms contributing to charged double pion electroproduction for the kinematics covered by our measurement. All differential and fully integrated cross sections obtained in our measurement can be reasonably described by the contributions from  $\pi\Delta$  isobar channels and direct double pion production mechanisms, established from phenomenological analysis of our data. The resonant contributions to all integrated and one-fold differential cross sections were determined from the data analysis.

The data also allowed us to determine cross sections and amplitudes for isobar channels, offering valuable information for nucleon resonance studies in an analysis of the single and double pion electroproduction within the framework of an advanced coupled-channel approach currently under development in the Excited Baryon Analysis Center (EBAC) at Jefferson Lab [25,27]. Successful description of experimental

data on all available observables in these exclusive channels with completely different nonresonant mechanisms, employing a common set of  $N^*$  electrocouplings, is vital to obtaining reliable data on transition helicity amplitudes to the  $P_{11}(1440)$  and  $D_{13}(1520)$  states.

### ACKNOWLEDGMENTS

We acknowledge the outstanding efforts of the staff of the Accelerator and Physics Divisions at Jefferson Lab that made this experiment possible. This work was supported in part by the Skobeltsyn Institute of Nuclear Physics and Physics Department at Moscow State University, the US Department of Energy and the National Science Foundation, the UK Engineering and Physical Science Research Council, the Istituto Nazionale di Fisica Nucleare, the French Centre National de la Recherche Scientifique, the French Commissariat à l'Énergie Atomique, and the Korean Science and Engineering Foundation. Jefferson Science Associates (JSA) operates the Thomas Jefferson National Accelerator Facility for the US Department of Energy under Contract DE-AC05-06OR23177.

### APPENDIX: KINEMATIC VARIABLES FOR FIVE-DIFFERENTIAL $2\pi$ PRODUCTION CROSS SECTIONS

In this Appendix, we present the final state kinematics for the second choice of variables defined in Sec. V A. Since all momenta are measured in the laboratory frame, first we boost the three-momenta of the final state particles in the c.m. frame. All three-momenta used below, if not specified otherwise, are defined in the c.m. frame.

$M_{\pi^+\pi^-}$ ,  $M_{\pi^+p}$ , and  $M_{\pi^-p}$  invariant masses were related to the four-momenta of the final particles as

$$\begin{aligned} M_{\pi^+\pi^-} &= \sqrt{(P_{\pi^+} + P_{\pi^-})^2}, \\ M_{\pi^+p'} &= \sqrt{(P_{\pi^+} + P_{p'})^2}, \\ M_{\pi^-p'} &= \sqrt{(P_{\pi^-} + P_{p'})^2}, \end{aligned} \quad (\text{A1})$$

where  $P_i$  ( $i = \pi^-, \pi^+, p$ ) stands for the final state particle four-momenta.

The angle  $\theta_{\pi^-}$  between the three-momentum of the initial photon and the final state  $\pi^-$  in the c.m. frame was calculated as

$$\theta_{\pi^-} = \arccos \left( \frac{(\vec{P}_{\pi^-} \cdot \vec{P}_{\gamma})}{|\vec{P}_{\pi^-}| |\vec{P}_{\gamma}|} \right). \quad (\text{A2})$$

The angle  $\varphi_{\pi^-}$  was determined as

$$\varphi_{\pi^-} = \arctan \left( \frac{P_{y\pi^-}}{P_{x\pi^-}} \right), \quad P_{x\pi^-} > 0, \quad P_{y\pi^-} > 0, \quad (\text{A3})$$

$$\varphi_{\pi^-} = \arctan \left( \frac{P_{y\pi^-}}{P_{x\pi^-}} \right) + 2\pi, \quad P_{x\pi^-} > 0, \quad P_{y\pi^-} < 0, \quad (\text{A4})$$

$$\varphi_{\pi^-} = \arctan \left( \frac{P_{y\pi^-}}{P_{x\pi^-}} \right) + \pi, \quad P_{x\pi^-} < 0, \quad P_{y\pi^-} < 0, \quad (\text{A5})$$

$$\varphi_{\pi^-} = \arctan \left( \frac{P_{y\pi^-}}{P_{x\pi^-}} \right) + \pi, \quad P_{x\pi^-} < 0, \quad P_{y\pi^-} > 0, \quad (\text{A6})$$

$$\varphi_{\pi^-} = \pi/2, \quad P_{x\pi^-} = 0, \quad P_{y\pi^-} > 0, \quad (\text{A7})$$

$$\varphi_{\pi^-} = 3\pi/2, \quad P_{x\pi^-} = 0, \quad P_{y\pi^-} < 0. \quad (\text{A8})$$

The calculation of the angle  $\alpha_{(\pi^-p)(\pi^+p')}$  between planes A and B (see Fig. 7) is more complicated. First we determine two auxiliary vectors  $\vec{\gamma}$  and  $\vec{\beta}$ . The vector  $\vec{\gamma}$  is the unit vector perpendicular to the  $\vec{P}_{\pi^-}$  three-momentum, directed toward the vector  $-\vec{n}_z$  and situated in the plane composed by the virtual photon three-momentum and the  $\pi^-$  three-momentum  $\vec{P}_{\pi^-}$  (see Fig. 7).  $\vec{n}_z$  is the unit vector directed along the  $z$  axis (see Fig. 7). The vector  $\vec{\beta}$  is the unit vector perpendicular to the three-momentum of  $\pi^-$ , directed toward the  $\pi^+$  three-momentum  $\vec{P}_{\pi^+}$  and situated in the plane composed of the  $\pi^+$  and  $p'$  three-momenta. Note that the three-momenta of the  $\pi^+$ ,  $\pi^-$ , and  $p'$  are in the same plane, since in the center-of-mass their total three-momentum should be equal to zero. Then the angle between the two planes  $\alpha_{(\pi^-p)(\pi^+p')}$  is

$$\alpha_{(\pi^-p)(\pi^+p')} = \arccos(\vec{\gamma} \cdot \vec{\beta}), \quad (\text{A9})$$

with the arccos function running between zero and  $\pi$ , and the angle between planes A and B running from zero to  $2\pi$ . To determine  $\alpha$  in a range between  $\pi$  and  $2\pi$ , we look at the relative orientation of the vector  $\vec{P}_{\pi^-}$  and vector product  $\vec{\delta}$  for the auxiliary vectors  $\vec{\gamma}$  and  $\vec{\beta}$ :

$$\vec{\delta} = \vec{\gamma} \times \vec{\beta}. \quad (\text{A10})$$

If  $\vec{\delta}$  is collinear to  $\vec{P}_{\pi^-}$ ,  $\alpha_{(\pi^-p)(\pi^+p')}$  is determined from Eq. (A9). In the case of anticollinear vectors  $\vec{\delta}$  and  $\vec{P}_{\pi^-}$ ,

$$\alpha_{(\pi^-p)(\pi^+p')} = 2\pi - \arccos(\vec{\gamma} \cdot \vec{\beta}). \quad (\text{A11})$$

The vector  $\vec{\gamma}$  may be expressed through the particle three-momenta as

$$\begin{aligned} \vec{\gamma} &= a_\alpha(-\vec{n}_z) + b_\alpha \vec{n}_{P_{\pi^-}}, \\ a_\alpha &= \sqrt{\frac{1}{1 - (\vec{n}_{P_{\pi^-}} \cdot (-\vec{n}_z))^2}}, \\ b_\alpha &= -(\vec{n}_{P_{\pi^-}} \cdot (-\vec{n}_z)) a_\alpha, \end{aligned} \quad (\text{A12})$$

where  $\vec{n}_{P_{\pi^-}}$  is the unit vector directed along the  $\pi^-$  three-momentum (see Fig. 7). Taking scalar products  $(\vec{\gamma} \cdot \vec{n}_{P_{\pi^-}})$  and  $(\vec{\gamma} \cdot \vec{\gamma})$ , it is straightforward to verify that  $\vec{\gamma}$  is the unit vector perpendicular to  $\vec{P}_{\pi^-}$ .

The vector  $\vec{\beta}$  may be obtained as

$$\begin{aligned} \vec{\beta} &= a_\beta \vec{n}_{P_{\pi^+}} + b_\beta \vec{n}_{P_{\pi^-}}, \\ a_\beta &= \sqrt{\frac{1}{1 - (\vec{n}_{P_{\pi^+}} \cdot \vec{n}_{P_{\pi^-}})^2}}, \\ b_\beta &= -(\vec{n}_{P_{\pi^+}} \cdot \vec{n}_{P_{\pi^-}}) a_\beta, \end{aligned} \quad (\text{A13})$$

where  $\vec{n}_{P_{\pi^+}}$  is the unit vector directed along the  $\pi^+$  three-momentum. Again, taking scalar products  $(\vec{\beta} \cdot \vec{n}_{P_{\pi^-}})$  and  $(\vec{\beta} \cdot \vec{\beta})$ , it is straightforward to see that  $\vec{\beta}$  is the unit vector perpendicular to the  $\pi^-$  three-momentum. The angle  $\alpha_{(\pi^-p)(\pi^+p')}$  coincides

with the angle between the vectors  $\vec{\gamma}$  and  $\vec{\beta}$ . So, the scalar product  $(\vec{\gamma}\vec{\beta})$  allows determination of the angle  $\alpha_{(\pi^-\pi^+p')}$  in Eq. (A9).

The kinematic variables for other hadron assignments for the first, second, and third final state particle described above were evaluated in a similar way.

- 
- [1] V. D. Burkert, in *Electromagnetic Interactions and Hadronic Structure*, edited by F. Close, S. Donnachie, and G. Shaw, Cambridge Monographs on Particle Physics, Nuclear Physics and Cosmology No. 25 (Cambridge University, Cambridge, 2007), p. 77.
- [2] V. D. Burkert, *Prog. Part. Nucl. Phys.* **55**, 108 (2005).
- [3] V. Burkert and T. S.-H. Lee, *Int. J. Mod. Phys. E* **13**, 1035 (2004).
- [4] K. Joo *et al.*, *Phys. Rev. Lett.* **88**, 122001 (2002).
- [5] M. Ungaro *et al.*, *Phys. Rev. Lett.* **97**, 112003 (2006).
- [6] K. Joo *et al.*, *Phys. Rev. C* **68**, 032201 (2003).
- [7] K. Joo *et al.*, *Phys. Rev. C* **70**, 042201 (2004).
- [8] K. Joo *et al.*, *Phys. Rev. C* **72**, 058202 (2005).
- [9] H. Egiyan *et al.*, *Phys. Rev. C* **73**, 025204 (2006).
- [10] A. Biselli *et al.*, *Phys. Rev. C* **68**, 035202 (2003).
- [11] A. Biselli *et al.*, *Phys. Rev. C* **78**, 045204 (2008).
- [12] K. Park *et al.*, *Phys. Rev. C* **77**, 015208 (2008).
- [13] R. Thompson *et al.*, *Phys. Rev. Lett.* **86**, 1702 (2001).
- [14] H. Denizli *et al.*, *Phys. Rev. C* **76**, 015204 (2007).
- [15] P. Ambrozewicz *et al.*, *Phys. Rev. C* **75**, 045203 (2007).
- [16] I. Aznauryan *et al.*, *Phys. Rev. C* **78**, 045209 (2008).
- [17] D. Carman *et al.*, *Phys. Rev. Lett.* **90**, 131804 (2003).
- [18] R. De Vita *et al.*, *Phys. Rev. Lett.* **88**, 082001 (2002).
- [19] G. Penner and U. Mosel, *Phys. Rev. C* **65**, 055202 (2002).
- [20] K. Wacker *et al.*, *Nucl. Phys.* **B144**, 269 (1978).
- [21] M. Ripani *et al.*, *Phys. Rev. Lett.* **91**, 022002 (2003).
- [22] CLAS Physics Data Base, see <http://clasweb.jlab.org/physicsdb/>.
- [23] T. Sato and T.-S. H. Lee, *Phys. Rev. C* **63**, 055201 (2001).
- [24] B. Julia-Diaz *et al.*, *Phys. Rev. C* **77**, 045205 (2008).
- [25] A. Matsuyama, T. Sato, and T.-S. H. Lee, *Phys. Rep.* **439**, 193 (2007).
- [26] T. S.-H. Lee, *J. Phys. Conf. Ser.* **69**, 012013 (2007).
- [27] T. S.-H. Lee and L. C. Smith, *J. Phys. G* **34**, S83 (2007).
- [28] S. Capstick and B. D. Keister, *Phys. Rev. D* **51**, 3598 (1995).
- [29] F. Cano and P. González, *Phys. Lett.* **B431**, 270 (1998).
- [30] I. G. Aznauryan, *Phys. Rev. C* **76**, 025212 (2007).
- [31] T. Ebata and K. E. Lassia, *Phys. Rev.* **183**, 1425 (1969).
- [32] V. I. Mokeev, V. D. Burkert *et al.*, in *NSTAR2005: Proceedings of the Workshop on the Physics of Excited Nucleons*, edited by S. Capstick, V. Crede, and P. Eugenio (World Scientific, Singapore, 2006).
- [33] V. I. Mokeev and V. D. Burkert, *J. Phys. Conf. Ser.* **69**, 012019 (2007).
- [34] T. Kitagaki *et al.*, *Phys. Rev. D* **34**, 2554 (1986).
- [35] J. Bell *et al.*, *Phys. Rev. Lett.* **41**, 1008 (1978).
- [36] D. Allasia *et al.*, *Nucl. Phys.* **B343**, 285 (1990).
- [37] C. Alexandrou, T. Leontiou, J. W. Negele, and A. Tsapalis, *Phys. Rev. Lett.* **98**, 052003 (2007).
- [38] U. Thoma, *Int. J. Mod. Phys. A* **20**, 280 (2005).
- [39] A. Anisovich, E. Klempt, A. Sarantsev, and U. Thoma, *Eur. Phys. J. A* **24**, 111 (2005).
- [40] D. Luke and P. Söding, *Multiple Pion Photoproduction in the s Channel Resonance Region*, Springer Tracts in Modern Physics, Vol. 59 (Springer, New York, 1971).
- [41] J. A. Gomez Tejedor and E. Oset, *Nucl. Phys.* **A600**, 413 (1996).
- [42] J. C. Nacher *et al.*, *Nucl. Phys.* **A674**, 205 (2000).
- [43] L. Y. Murphy and J.-M. Laget, DAPNIA-SPHN-96-10 (March 1996).
- [44] W. Roberts and A. Rakotovao, JLAB-TH-97-01, hep-ph/9708236.
- [45] W. Roberts and T. Oed, *Phys. Rev. C* **71**, 055201 (2005).
- [46] M. Hirata, N. Katagiri, and T. Takaki, *Phys. Rev. C* **67**, 034601 (2003).
- [47] A. Fix and H. Arenhovel, *Eur. Phys. J. A* **25**, 115 (2005).
- [48] G. V. Fedotov *et al.*, *Bull. Russian Acad. Sci. Phys.* **71**, 328 (2007).
- [49] M. Ripani *et al.*, *Nucl. Phys.* **A672**, 220 (2000).
- [50] V. Mokeev *et al.*, *Phys. At. Nucl.* **64**, 1292 (2001).
- [51] V. Mokeev *et al.*, *Phys. At. Nucl.* **66**, 1322 (2003).
- [52] I. G. Aznauryan, V. D. Burkert, G. V. Fedotov, B. S. Ishkhanov, and V. I. Mokeev, *Phys. Rev. C* **72**, 045201 (2005).
- [53] V. D. Burkert *et al.*, *Phys. At. Nucl.* **70**, 427 (2007).
- [54] V. I. Mokeev *et al.*, in *NSTAR2007: Proceedings of the 11th Workshop on the Physics of Excited Nucleons, 5–8 September 2007, Bonn, Germany*, edited by H.-W. Hammer, V. Kleber, U. Thoma, and H. Schmieden (Springer, New York, 2008).
- [55] V. I. Mokeev *et al.*, arXiv:0809.4158.
- [56] B. Mecking *et al.*, *Nucl. Instrum. Methods Phys. Res. A* **503**, 513 (2003).
- [57] M. D. Mestayer *et al.*, *Nucl. Instrum. Methods Phys. Res. A* **449**, 81 (2000).
- [58] G. Adams *et al.*, *Nucl. Instrum. Methods Phys. Res. A* **465**, 414 (2001).
- [59] E. S. Smith *et al.*, *Nucl. Instrum. Methods Phys. Res. A* **432**, 265 (1999).
- [60] M. Amarian *et al.*, *Nucl. Instrum. Methods Phys. Res. A* **460**, 239 (2001).
- [61] [http://www.jlab.org/~golovach/www\\_eg/index.html](http://www.jlab.org/~golovach/www_eg/index.html).
- [62] E. Byckling and K. Kajantie, *Particle Kinematics* (John Wiley & Sons Inc., New York, 1973).
- [63] P. E. Bosted, *Phys. Rev. C* **51**, 409 (1995).
- [64] E. Amaldi, S. Fubini, and G. Furlan, *Pion Electroproduction*. Springer Tracts in Modern Physics, edited by G. Hohler (Springer-Verlag, Berlin, 1979), Vol. 83.
- [65] C. Hadjidakis *et al.*, *Phys. Lett.* **B605**, 256 (2005).
- [66] L. W. Mo and Y. S. Tsai, *Rev. Mod. Phys.* **41**, 205 (1969).
- [67] A. Afanasev, I. Akushevich, V. Burkert, and K. Joo, *Phys. Rev. D* **66**, 074004 (2002).
- [68] A. Braghieri *et al.*, *Phys. Lett.* **B363**, 46 (1995).
- [69] C. Wu *et al.*, *Eur. Phys. J. A* **23**, 317 (2005).
- [70] A. Kiswandhi *et al.*, *J. Phys. Conf. Ser.* **69**, 012018 (2007).
- [71] I. G. Aznauryan, V. D. Burkert, H. Egiyan, K. Joo, R. Minehart, and L. C. Smith, *Phys. Rev. C* **71**, 015201 (2005).